ETH Zürich
Department of Civil, Environmental and Geomatic Engineering
Institute of Environmental Engineering

MSc Thesis
FS 2017

Impact of water saturation on chemical reactions in porous media fronts

Mayumi Hamada

Supervisors:

Dr. Joaquin Jiménez-Martínez (EAWAG and ETH Zürich)

Prof. Pietro de Anna (University of Lausanne)

Zürich, August, 2017

Abstract

The heterogeneous velocity field found in porous media induces a deformation of the solute concentration field into a lamella-like topology. Mixing resulting form this process is driven by advection, dispersion and diffusion of solute concentration. At small scale, reactive flow processes in those environments reveal a kinetic significantly different from what is happening at Darcy scale due to non well-mixed conditions found within pores. We perform two types of experiment where the displacement of the front between two solutions is visualized in a synthetic porous medium using a computer controlled camera. One experiment is a conservative flow experiment: we record the displacement of the concentration field of a conservative tracer to measure the evolution of the front geometry. We observe a linear increase of the front length with time and we show this growth to be proportional to the applied flow rate. The second experiment is a reactive flow experiment: we consider a fast bimolecular chemiluminescent reaction between two solutions A and B; the porous medium is saturated with B and A is injected, the reaction happens at the interface of A and B and produces light. The reaction rate between A and B is given by the total light intensity measured per unit time. With this experiment we study the impact of flow rate and saturation degree on the evolution of the reaction rate. We verify that the measured light intensity can be well predicted by a model describing reaction rate as a function of the front geometry evolution, where diffusion and stretching compete in dissipating and respectively spreading the concentration gradient. In this framework we show that, for the four saturation degrees tested, the reaction rate is proportional to the flow rate, and for the two lowest flow rates it is inversely proportional to the saturation degree.

Eidgenössische Technische Hochschule Zürich
Swiss Federal Institute of Technology Zurich

Declaration of originality

The signed declaration of originality is a component of every semester paper, Bachelor's thesis, Master's thesis and any other degree paper undertaken during the course of studies, including the respective electronic versions.

Lecturers may also require a declaration of originality for other written papers compiled for their courses.

I hereby confirm that I am the sole author of the written work here enclosed and that I have compiled it in my own words. Parts excepted are corrections of form and content by the supervisor.

Title of work (in block letters):

IMPACT OF WATER SATURATION ON CHEMICAL REACTIONS IN POROUS MEDIA FRONTS

Authored by (in block letters):

For papers written by groups the names of all authors are required.

Name(s):	**First name(s):**
HAMADA	MAYUMI

With my signature I confirm that

- I have committed none of the forms of plagiarism described in the 'Citation etiquette' information sheet.
- I have documented all methods, data and processes truthfully.
- I have not manipulated any data.
- I have mentioned all persons who were significant facilitators of the work.

I am aware that the work may be screened electronically for plagiarism.

Place, date	**Signature(s)**
Zürich, the 9th of August 2017	

For papers written by groups the names of all authors are required. Their signatures collectively guarantee the entire content of the written paper.

Contents

1 Introduction

1.1 Reactions in geologic environment

The underground is composed of several compartments, including soil, vadose zone and aquifer, in which several phases (i.e. solids-rock, fluids and gases) and living organisms coexist in close interaction as schematically shown in Figure 1 on the left. This environment is called the critical zone: where biotic and abiotic components are coupled to drive the elements and energy cycle that are controlled by small scale physical and biochemical processes (Figure 1, on the right). Land-atmosphere or river-aquifer boundaries have been identified as interfaces where mass and energy fluxes take place leading to biological and chemical activities disproportionately higher than their surroundings [1]. These interfaces are also characterized by a wide fluid velocity heterogeneity, multi-phase flows, high spatial variability and temporal persistence of gradients of chemical and biological species and reactions taking place mainly where these gradients are important.

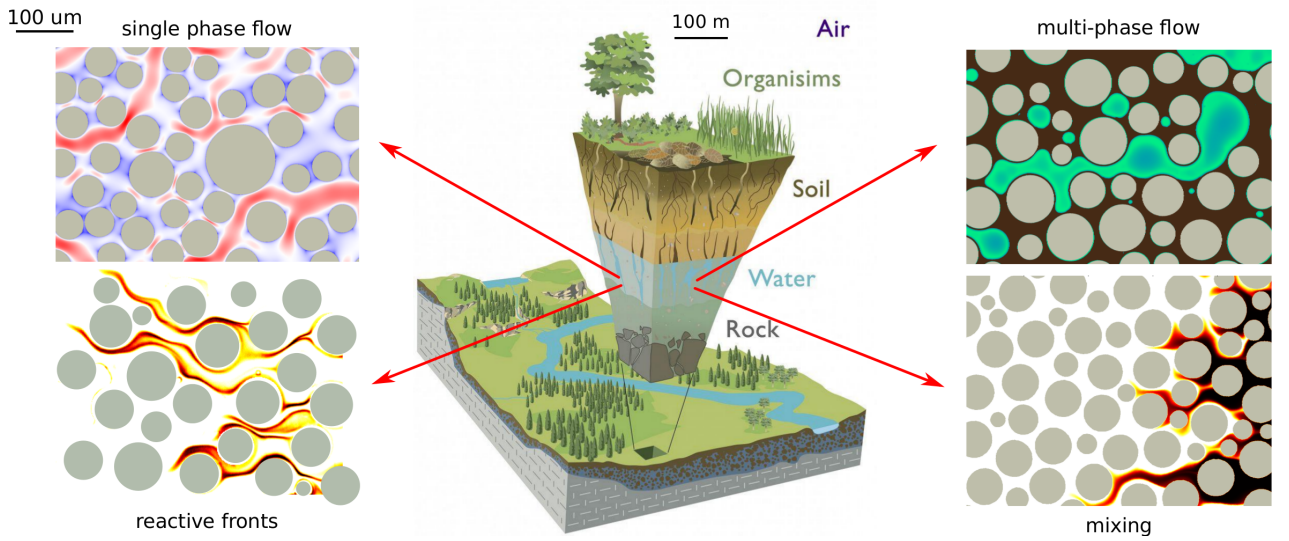

Figure 1: Left: a representation of a large scale (∼100 m) near-surface environment [2]. Right: visualization of processes taking place at small scale (∼ 100 μm), including saturated and unsaturated flow, mixing and reaction front.

The masses experiencing transport through these interfaces are not only transferred and stored, but they are often biologically and chemically transformed over a range of spatial and temporal scales, driven by the local geology, rain seasons or discharge periods (e.g. [3]). Typical reactions taking place in such environments include oxidation of organic molecules, aerobic degradation, chemical precipitation of heavy metals, release of natural contaminants such as arsenic, or anthropogenic ones such as nitrate, or the dissolution of CO_2 and carbonate rocks (e.g. [4, 5]).

The subsurface waters displacement play a key role in governing hydrological and geochemical fluxes which affect the chemical and biological dynamics of a number of important environmental and industrial processes, including contaminant transfer and accumulation in soils (e.g. [6]), micro-organism nutrient cycles (e.g. [7]), CO_2 injection or enhanced oil recovery in geological reservoirs (e.g. [8]). Particularly challenging is

the characterization and modeling of reactive transport that requires the coupling of processes such as flow, transport and chemical reactions due to its non linear dependence on the local concentrations [9, 10, 11]. For this reason, reactive transport at large and small scales remains a largely open question [3, 12].

Moreover, in the context of hydrology, chemical reactions of particular interest are those between the constituents of the soil and solutes dissolved in water flowing through it including, for example, dissolution reactions responsible for karst formations and biochemical reactions that control the dynamics of bacteria population in soil (e.g. denitrification, biodegradation). It has to be noted that geologic media reactivities are characterized by a wide range of temporal scales, from shorter than hours to several millions of years, and spatial scales, from less than a millimeter (sub-pore) to hundreds of kilometers (drainage basin) across which the observed reactivity can change over several orders of magnitude [3]. This huge variability has been associated to the existence of hot-spots and hot-moments where the medium reactivity is very high, also due to the presence of fluid motion and the dynamics that it originates.

1.2 Subsurface flows

1.2.1 Governing equations

The physics of the fluids flow is controlled by *momentum conservation law*: the local momentum variation in a time unit, must correspond to an equal variation of momentum in a space unit. Mathematically, the momentum conservation leads to a set of partial differential equations, called Navier-Stokes, for the local velocity field (which correspond to the force balance):

$$\frac{\partial \vec{u}}{\partial t} - \vec{u} \cdot \nabla \vec{u} = \rho \, \vec{g} - \nabla p + \mu \nabla^2 \vec{u} \tag{1}$$

where $\vec{u}$ is the local fluid velocity, ρ its density, μ its dynamics viscosity and p the local pressure [13]. The left hand side of Eqs. (1) represents the total, or material, derivative of the local velocity whose second term $-\vec{u} \cdot \nabla \vec{u}$ represents the inertial forces. On the right hand side of Eqs. (1), we find the sum of the body forces (here only gravity) and the surface forces acting on each medium elementary volume. The latter is composed by the pressure gradient and the shear force that, for Newtonian fluids like water, is proportional to $\nabla^2 \vec{u}$ through the fluid dynamic viscosity and, thus, it is also called viscous force.

These non linear partial differential equations can be simplified when the inertial forces can be neglected, if compared to viscous ones, for an incompressible fluid ($\nabla \cdot \vec{u} = 0$). The ratio between these two forces is quantified by the Reynolds number, a dimensionless quantity defined as $Re = \frac{u \rho \lambda}{\mu}$, where u is the average fluid velocity and λ a characteristic length scale of the considered flowing system. When a system is characterized by a low Reynolds number, i.e. $Re < 1$, the Eqs. (1) can be simplified into the so called Stokes equation:

$$\nabla p = \rho \, \vec{g} + \mu \nabla^2 \vec{u}. \tag{2}$$

where $\vec{u}$ is stationary and the fluid incompressible. In such conditions the flow is characterized by the so called laminar regime, in which fluids elements flow parallel to each other as lamina, very thin layer of a material [14]. Even tough Stokes flows are characterized by low velocities (the Reynolds number is small), the flow heterogeneity can be relevant, as discussed in the next section.

1.2.2 The heterogeneity of natural flows

With flow heterogeneity we refer to the fact that the fluid motion is variable in space: a concept intuitively clear for open systems, like surface or atmospheric flows, as qualitatively shown by the result of a numerical simulation of global oceanic flows displayed in Figure 2 on the left. In such open flows water can move freely, without encountering solid immobile obstacles, with characteristic velocities u on the order of 1 m/s and characteristic length scale λ being equal or larger than $1 - 10^2$ m [10]. For these systems the Reynolds number is typically high, $Re \gg 1$, the flow is typically chaotic or turbulent [13] and characterized by spatial variability. The smallest spatial scale over which velocity variations are observable in turbulent systems is defined by the Kolmogorov scale $\eta = (\frac{\nu^3}{\epsilon})^{1/4}$, below which the fluid energy is dissipated since viscosity cannot be neglected [13]. This length scale depends on the energy dissipation rate ϵ and on the fluid viscosity ν: for oceanic systems the value of η is on the order of 1 mm [15]. In Figure 2 the left box represents a virtual zoom into a oceanic turbulent flow displacing, deforming and stretching a patch of a chemical those evolution has been simulated [16]. The solutes volume is deformed by the flow field and get organized in elongated and very thin structures: the thickness of such structures is of the order of η, below which transported solute concentration gradients are not observable.

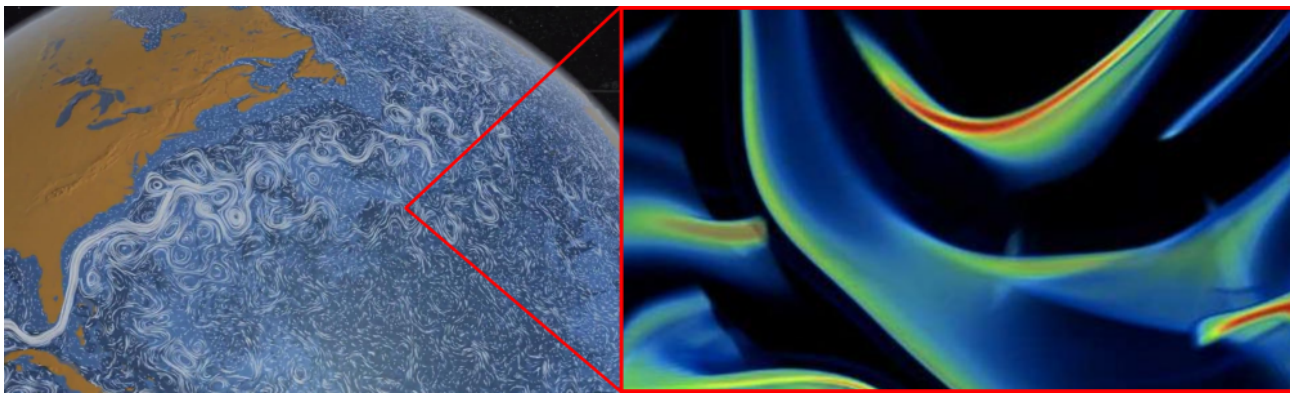

Figure 2: Left: a simulated oceanic flow (source: NASA). Right: the filament organization of a stretched patch of a tracer in a turbulent flow (image from [16])

In soils and aquifers the overall picture is dramatically different: the motion of fluids is not free, they are confined in much smaller spaces typically of size λ ranging between $10^{-6} - 10^{-2}$ m [14]. Thus, fluids moving within such confined structures, characterized by distances λ, are forced to pass between solid and impermeable obstacles: there, typical velocities are on the order of $1 - 100\,\mu$m/s, much lower than their open flow counterparts. Therefore, these confined flows are characterized by much smaller Reynolds numbers, typically $Re < 10^{-1}$. Hydrologist have studied such flows and the consequent flow-driven processes, like solutes trans-

port, observing that the spatial variability of the fluid motion plays a relevant role, but it typically appears, in practical field applications, at scales where the solid structure of the host medium is not resolved and the fluid motion is represented by an averaged Darcy-like flow through a permeability field that represents and quantify the ability of the medium to transfer fluid. Therefore, we are often led to believe that confined flows are quite homogeneous at small-scales (i.e. mm or below) and their heterogeneity appears only at larger scales where the geologic medium changes its macroscopic properties (like permeability or porosity).

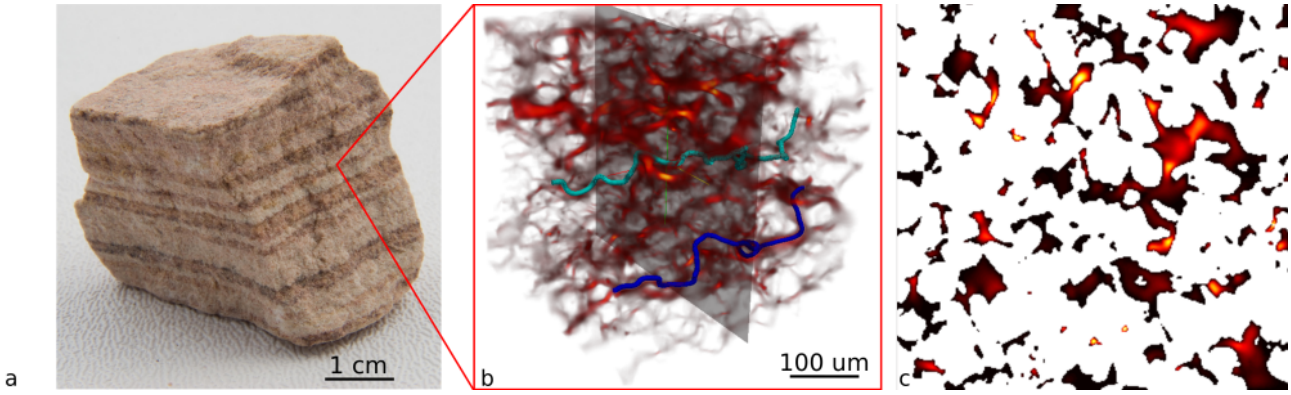

Figure 3: a) A sandstone, b) 3D flow field through a Berea-sandstone superposed to two fluid particles trajectories (in light and dark blue), and c) a cross section of image b showing the spatial heterogeneity of velocity within the pore space [17].

However, recent research has proven the presence of a very rich flow structure and heterogeneity at small scale. Figure 3.a represents a sample of sandstone; a numerical simulation of the Stokes flow (modulus of the velocity field) through such a natural structure is represented in Figure 3.b and .c (a cross section of the 3D image). The velocity variability characterizes fluid motion through the considered confined structures even at very small-scales and also for very low Reynolds numbers [17, 18, 19]. Other studies have proven that such property of porous media flows is responsible for the so called anomalous transport, characterized by non-Fickian dispersion or long temporal tailing of breakthrough curves [20, 17]. These behaviors also lead to the breakdown of the main hypothesis behind the classical models for reactive transport: the well-mixed condition for the involved chemicals, as discussed below.

1.3 Mass transport and mixing by confined flows

Mixing is the result of mass transport and it is the ensemble of mechanisms that changes the spatial distribution of an heterogeneous system, to make it more homogeneous. Due to mixing, two or more given substances originally segregated into different volumes of space, tend to occupy the same volume (e.g. [21, 22]).

In other words, *a mixture is a transient state between the initial segregation of the constituents and their ultimate homogeneity* [24]. This concept is well represented in Figure 4, where two initially segregated drops of different ink are mixed [23]. As time goes on, the mixing mechanisms reduce the system heterogeneity until the two drops are fully homogenized and indistinguishable: all spatial heterogeneities are eliminated. With this

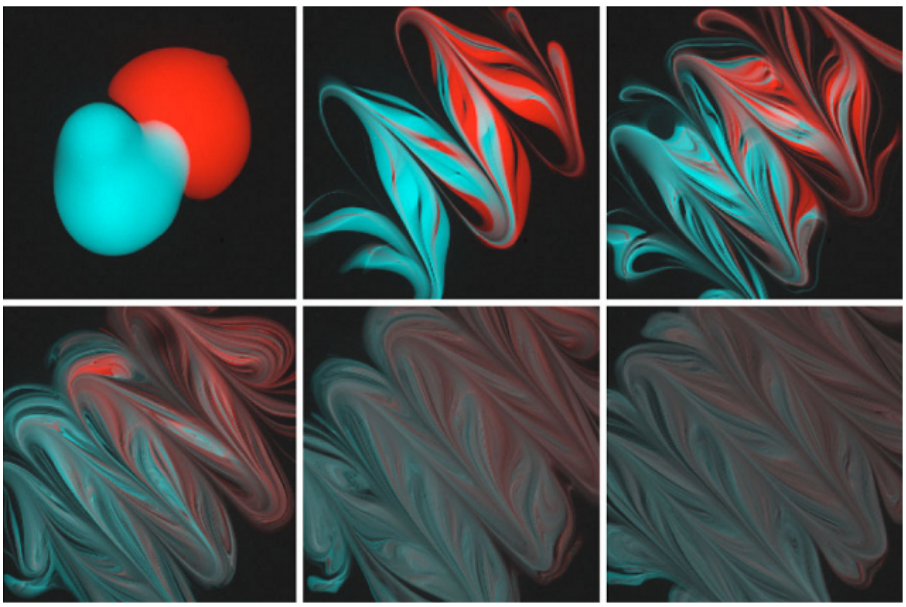

Figure 4: Mixing of two ink spots initially laid side by side. Image is taken from [23], where mixing process is described.

rigorous definition of mixing, it is now possible to quantitatively define the meaning of well-mixed condition over a spatial scale λ, required by the mass action law to describe the velocity of chemical reactions (as discussed in details in the next section): over λ the concentration gradients must be zero (or negligible). In other words, λ is the largest scale over which it is not possible to observe any concentration variations. All variability at smaller scale than λ is considered to be already homogenized by mixing. In geologic media the scale λ is much smaller than the size L of the considered system, implying that the mixing may limit the system reactivity, as discussed below.

The mechanic processes responsible for mixing in porous media are advection (discussed in the previous subsection) and molecular diffusion (associated to thermal fluctuations). The conservation of mass controls the spatio-temporal evolution of a solute concentration c in a flow field $\vec{u}$:

$$\frac{\partial c}{\partial t} = -\vec{u} \cdot \nabla c + D\nabla^2 c, \tag{3}$$

where D is the molecular diffusion coefficient [14]. We define the dimensionless Péclet number $Pe = \frac{\lambda \overline{v}}{D}$ that takes into account the effective ratio between advection and diffusion time scales over a given length λ. Systems characterized by high Pe are controlled by advection, while a small Pe describes diffusion dominated situations. This appears clear by rescaling time in Eq.(3) by the characteristic advection time over a pore space as $t' = \lambda/\overline{u}$ and space as $x' = x/\lambda$, obtaining:

$$\frac{\partial c}{\partial t'} = -\frac{\vec{u}}{\overline{u}} \cdot \nabla' c + \frac{1}{Pe}\nabla'^2 c. \tag{4}$$

These two processes are coupled in contributing to the degree of mixing. If, on one hand, heterogeneous

advection spreads the solutes along the local direction of the fluid flow, increasing their spatial variability and gradients, on the other hand, diffusion homogenizes their spatial distribution (e.g. [21]). At large scale, this interaction between heterogeneous advection and diffusion is typically lumped in a dispersion coefficient to describe solutes spreading as a proxy for an effective mixing at large, geologic, scale (e.g. [25]). However, spreading must be differentiated from mixing and an accurate description of the mixing processes and its dynamics is necessary when reactions between solutes are involved [22], as discussed below.

1.4 The fate of chemicals: the reaction kinetics

In our daily experience chemical reactions are not instantaneously transformed into products: for instance the dissolution of an aspirin tablet in water or a spoon of sugar in a cup of coffee. Such transformations can take place only between molecules (like the solid aspirin and the liquid water) that are close enough to exchange electrons forming and breaking chemical bonds [26]. In other words, if the involved reactants are placed at large distance they cannot meet, by collision, and thus no reaction between them is possible ([9]). Of course, a chemical reaction is a very complex sequence of atomic-level processes that depends on many environmental parameters like temperature, pressure, pH, etc. Here, we consider a reaction as a black box containing the ensemble of processes that leads to the transformation of one set of reactants to a set of products through changes that strictly involve a short range interaction. Therefore, this observed short range nature of the chemical interaction [26] requires transport mechanisms at small, molecular, scale in order to produce collisions and thus reactions ([9, 11]).

Many non chemical phenomena are based on the short range interactions between particles or agents: for instance, the population dynamics of biological species (e.g. [**?**, 27]), ecological activity (e.g. [28]) or social behavior (e.g. [29]). In this context, reactive processes are ubiquitous in our daily experience, in nature and many industrial applications, for which it is very important to know, describe and predict the velocity.

The kinetics of a chemical reaction is a measurement of the degradation velocity of the involved reactants, and, beside the environmental parameters like temperature or pH, it depends on the mass ratio of the involved reactants. To formally describe reactions, chemical equations are typically used: they represent the ratio of the involved chemicals masses that are needed to produce one reaction (e.g. [26]). For instance, let's consider the reaction that occur between N chemical species with α_i molecules for the chemical species X_i for $i = 1, \dots N$:

$$\alpha_1 X_1 + \alpha_2 X_2 + \dots \alpha_N X_N \rightarrow \text{products at a given rate} \tag{5}$$

where the numbers α_i are the so called stoichiometric coefficients and represent the number of molecules of the chemical i that should be involved to produce a single reaction. A general law that predicts the reaction rate as a function of concentrations c_i of involved reactants X_i is the well known **mass action law**. This law states that the **rate of a reaction is proportional to the product of the concentration of the involved**

chemicals each one elevated to representative stoichiometric coefficient:

$$\text{reaction rate} = k c_1^{\alpha_1} c_2^{\alpha_2} \dots c_N^{\alpha_N} \tag{6}$$

where the proportionality constant k is the so called reaction rate constant. **The fundamental hypothesis behind this law is that the involved chemicals X_i are diluted and well mixed**. As defined in the previous section, this implies that everywhere in the considered domain the reactants concentration must have the same value. Thus, spatial effects are absent, or can be neglected, and the time evolution of the concentrations of all involved chemicals is provided by a system of ordinary differential equations, called rate equations, derived from the previous mass action law Eq. 6 (e.g. [11, 26]):

$$\frac{dc_i}{dt} = -\alpha_i k c_1^{\alpha_1} c_2^{\alpha_2} \dots c_N^{\alpha_N} \tag{7}$$

This dynamical system can be solved through deterministic (e.g. [30]), or stochastic approaches for well mixed systems.

If reactions are very fast compared to the mixing processes, the chemicals are locally depleted and the reaction, locally, stops: only a new mixing of reactants can allow reactions to take place again. Thus, mixing processes play an important role and can dominate the kinetics of a system characterized by a high reaction rate (e.g. [9, 11, 31, 32, 33, 34]).

In this master thesis we investigate a mixing limited (fast) bimolecular reaction $A + B \longrightarrow C$ taking place between two chemicals, A and B, that are moving, one displacing the other, in an unsaturated porous material. The goal is to understand the impact of incomplete mixing on global reaction rate in porous media flows.

1.4.1 Kinetics of a well-mixed fast bimolecular reaction

As mentioned above, the kinetics of a reaction is quantified in terms of the mass action law, stating that the dynamics of the change in the reactants concentration is proportional to the product of the involved reactants concentration, each elevated to the individual stoichiometric coefficient appearing in the chemical equation. The reaction we consider here is irreversible and binary $A + B \longrightarrow C$ (the stoichiometric coefficient is 1 for both reactants): thus, its kinetics is described by

$$\frac{dc_A}{dt} = -k\, c_A\, c_B \tag{8}$$

$$\frac{dc_B}{dt} = -k\, c_A\, c_B \tag{9}$$

which is a system of two coupled non linear differential equations.

If the initial concentration of the B reactant is much larger than the concentration of A, i.e. $c_{B0} \gg c_{A0}$, c_B

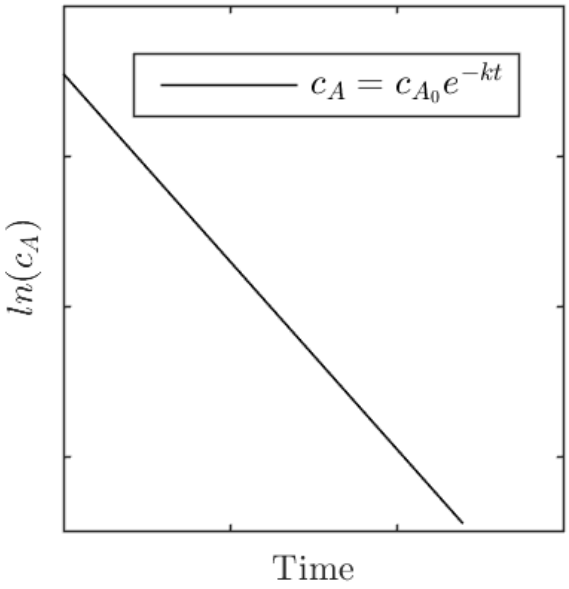

Figure 5: Solution for an exponential decay of a chemical A concentration c_A; the reaction follow the rate law $\frac{dc_A}{dt} = -k\, c_A$ where the rate constant k is in s^{-1}.

can be considered as a constant since its concentration is not going to change much due to the initial large disproportion with respect to the amount of A. Therefore, the reaction can be approximate by a first order decay:

$$\frac{dc_A}{dt} = -k\, c_A\, c_B \sim -k'\, c_A \tag{10}$$

$$\frac{dc_B}{dt} = \frac{dc_A}{dt} \ll C_{B0}, \qquad \forall t, \tag{11}$$

where $k' = kc_B$. In this case the Eq.(10) can be exactly solved:

$$c_A(t) = c_{A0}\, e^{-k'\, t} \tag{12}$$

$$c_B(t) \sim c_{B0} \quad \text{is nearly constant.} \tag{13}$$

Figure 5 gives an example of the solution of a first order decay of a chemical.

In conclusion, for the case in which one of the two reactants is much more concentrated than the other and that the two are well mixed, the less concentrated one will decay exponentially, while the other will keep its initial value since its depletion, equal to the one of the other chemical, is too small to affect its overall concentration. This conclusion holds in well mixed conditions: how will the reaction kinetics change if the system is characterized by incomplete mixing?

1.5 Reactions at mixing front

In many physical systems, the reactants are not well mixed at the scale λ at which the observation is made: this has an important impact on the measured reaction rate, as reported for a range of natural systems, from turbulent and chaotic flows ([10, 9, 11]) to transport in porous and fractured media ([12, 35, 36]). We consider the fast irreversible bimolecular reaction $A + B \longrightarrow C$ taking place at the front between two reactants A and B displaced by the heterogeneous flow field $\vec{u}$ whose modulus is represented in Figure 6.a (numerical simulation [37]). The medium is initially saturated with the reactant B and at time $t = 0$ the reactant A is continuously injected from the left boundary, as shown in Figure 6.b: at the moving interface between the two reactants the product C is formed (Figure 6.c). The mass conservation for the reactants is given by Eq. 3 plus a reactive (sink) term given by the mass action law applied to each pixel that is considered to be well mixed by molecular diffusion:

$$\frac{\partial c_i}{\partial t} = -\vec{u} \cdot \nabla c_i + D\nabla^2 c - k c_A c_B \qquad i = A, B \tag{14}$$

While it is assumed that it exists a spatial scale, smaller than the pore size, at which the system is well mixed, it is clear that the pores are not well mixed and the invading reactant front is organized in complex fingers-like structure.

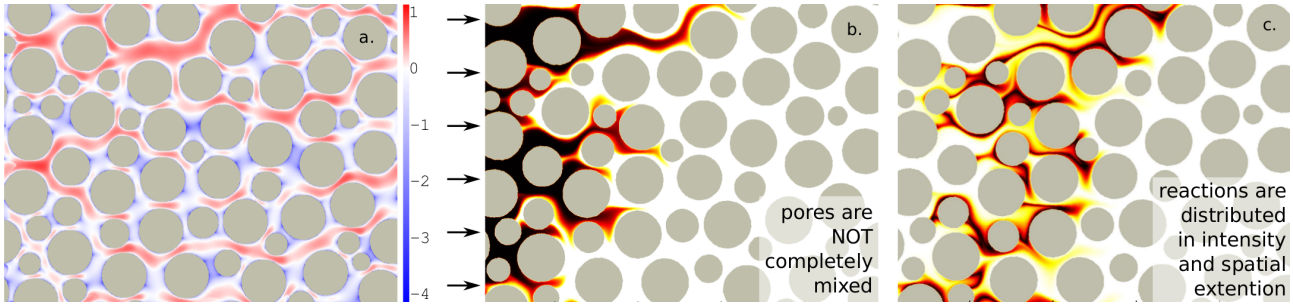

Figure 6: For a relatively simple grain geometry (gray disks): a) the normalized modulus u of the resulting laminar flow field is shown in a logarithmic scale $\log(u/\overline{u})$: the white color is associated to the average velocity $\overline{u}$, in red are the channels of high velocities and in blue stagnation zones. In this flow field b) a transported concentration field is organized in stretched lamellae where, reacting with a displaced solute, c) chemical reactions take place. This image is provided by Pietro de Anna's laboratory.

In natural media, the key mechanisms affecting the reaction front geometry are the ones described in the *mass transport and mixing* section: advective effects, that increase locally the reactant heterogeneity (by stretching, splitting due to solid obstacles and trapping in low velocity areas) and molecular diffusion, which tends to smooth out concentration gradients (e.g. [12, 24, 38, 33]). The relative importance of transport to reaction mechanisms is measured by the Damköhler number (Da) defined by the ratio of advection to reaction time scale. Due to the confined conditions for the flow, transport in porous media is typically characterized by low Péclet number values, $Pe \leq 1$, while Da varies depending on the precise chemical system under consideration. Here we consider a $Da \gg 1$.

Reactive transport models assume the existence of a length scale, the representative elementary volume, below which the reactants are considered well-mixed in order to describe the system in terms of mass conservation Eq. (14). Classical models assume that this scale is larger than a single pore, but evidence have shown that this cannot be always the case, even for simple geometries [31]. Thus, the global reaction kinetics cannot be quantified in terms of effective Fickian mass transfer rates. Only for relatively homogeneous fronts the chemical kinetics can be predicted using classical frameworks [39]. This is no longer true when the porous structure has some, even mild, heterogeneity.

The case considered here of $Da \gg 1$ for a simple irreversible bimolecular reaction in saturated porous media flows has received attention (e.g. [31, 37]), since it represents a paradigmatic example for reactive transport. Recent numerical simulations [37] and laboratory experiments [39] have shown the impact of incomplete mixing on the global reaction kinetics for a invading front in a saturated porous material. However, it is important to realize that most of the transformations occurring in natural conditions, are characterized by the presence of different phases, in other words under non saturated conditions.

1.6 The role of saturation

At pore-scale, if two phases coexist (e.g. water and air as in the unsaturated zone) the complex spatial distribution of the two phases complicates transport processes with respect to the fully saturated counterpart (i.e. the condition found in aquifers). The result is the development of regions of very low water velocity, including regions where water is trapped, and of preferential channels of high velocity [40]. This complex flow dynamics controls the distribution of dissolved chemicals and physico-chemical properties of water in the unsaturated zone (e.g. redox, pH). It also controls chemical reactions between the fluids or between the solids and the fluids, which further involves the spatio-temporal variability in the soil structure.

Figure 7 shows the main characteristics of flow in the unsaturated zone: strong fingering or preferential paths, with lateral diffusion from the edges of the fingers to immobile or stagnation zones, producing trapping of solute (e.g. contaminants). Two main transport processes are identified: dispersion and mixing.

Dispersion describes the continuous increase in time of the spatial extent of a solute plume. Dispersion is mostly a consequence of the heterogeneity in the velocity field and enhances concentration contrasts. However, dispersion in unsaturated porous media depends not only on flow velocity but also on saturation and the spatial distribution of the phases. This consideration relates to one of the major debate in the field, concerning the impact of water saturation on dispersion. Numerous studies have measured an increased dispersion with decreasing saturation [42]. Decreased dispersion with decreasing saturation has also been observed [43].

However, dispersion alone does not provide any information about the actual mixing of solutes (i.e. concentration distribution) within the plume, which affects potential chemical reaction processes [44]. Saturation-dependent mixing has been highlighted by studies focusing on the mixing of recently infiltrated water with

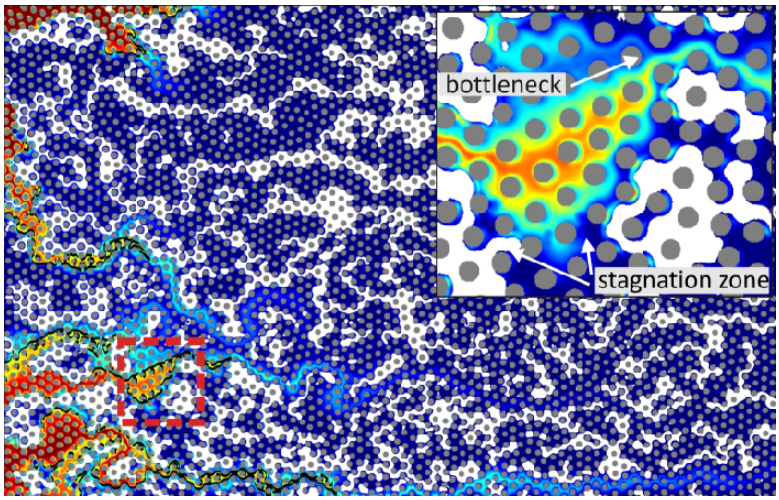

Figure 7: Normalized concentration field of fluorescein obtained in partially saturated conditions (water saturation, $w = 0.7$) for a continuous injection (air in white; grains in grey). In stagnation zones the tracer diffuse, while at bottlenecks formed between air clusters, coalescence of tracer fingers takes place [41].

old resident water [45]. The general view on unsaturated flows is that the existence of more pronounced preferential flow paths induces faster travel times and thus decreases the characteristic time of solute mixing and the total amount of chemical reactions [46]. However, this idea is not always correct, as flow channeling may also increase concentration gradients and thus diffusive mass transfer and reaction rates [41].

To date, technical limitations have prevented the visualization and quantification of the actual spatial distribution of reactivity in unsaturated porous media. Obtaining and characterizing the pore-scale reactivity for different phases saturation is the goal of this master thesis.

1.7 Microscopic investigation & project goal

In the past few decades numerical simulations have been widely used to obtain information on the spatial and temporal evolution of reactive subsurface system. The non linear nature of the reaction kinetics, as predicted by the discussed mass action law, implies that the numerical methods used must have a high spatial resolution, to properly capture the reactants variability, and value accuracy to keep low the numerical error that would be quickly amplified by the reactive term. Even more complicated is the situation in which the flow involves more than one phase and the interfacial forces must be taken into account.

In this work, we consider an experimental approach to quantify the reactive processes that take place at sub-pore scale at a displacing front in unsaturated conditions, in the spirit to understand the impact of saturation on the overall reaction kinetics.

Boreholes are our main source of information about subsurface processes, due to the solid and opaque nature of soils and rocks [6]. Novel small-scale imaging technologies have generated a large amount of new data providing highly detailed characterization of solid structures, flow and transport mechanisms as well as

reactive processes at scales ranging from micrometer to centimeter. We made use of a transparent replica of a porous material that allow for direct visualization, with a scientific camera, of the reactions that takes place at the invading front produced by an external pump.

2 Material and methods

The experiments carried out in this master thesis have been designed and performed to quantify the reaction kinetics taking place at a displacing front within porous media flows and for different phases saturation. Specifically, the work presented here is about water and air, but the developed set-up would also work for other fluids. We investigate the mixing-limited bimolecular reaction, described below, taking place at the displacing front in a porous medium. The novel set-up presented here is based on the exploitation of a *chemiluminescent* reaction: the interaction between two reactants that produces a photon, light. This reaction allows to directly quantify the amount and spatial distribution of the reactions taking place in a given time interval: the overall front kinetics. The total number of photons emitted by the front in a time interval is optically measured with a remotely controlled scientific camera.

Two types of experiment have been designed and performed: the conservative displacement of two distinguishable and miscible solutions and the reactive front between two reactants, one displacing the other. The first experiment is performed to measure the front length kinematics ($\Sigma(t)$) that is assumed to be representative of the reactive front kinematics for which the reaction kinetics is measured in the second experiment. The assumption that the two front lengths are similar is due to the fact that the molecular mass of the two transported solution (fluorescein and luminol) are similar and, therefore, similar is supposed to be their molecular diffusion coefficient.

2.1 Remotely controlled camera

The detection of the light emitted by the reaction is done with a scientific camera remotely controlled by a computer (a Dell workstation). The chemically produced photons reach the camera sensor where its active pixels convert the light signal into an electronic one, which will be recorded as a gray scale image by the computer. We used a *Ximea* camera whose sensor (ICX834) is a Coupled Charged Device (CCD) with 12 MegaPixel resolution: we have chosen camera mounting a CCD against a CMOS sensor because the first is producing less electronic noise (less signal to noise ratio) and less pixel correlation (the value of a pixel influences less the value of a neighboring pixel), resulting in sharper images.

The light emitted is focused into the camera sensor with a *Tamron* objective of fixed focal length of 50 mm and aperture of 2.1. The optics choice represents the best compromise between collecting as much light as possible (being as close as possible to the light source, i.e the reactive front) and obtaining *flat* images whose pixels are uniform in size: in other words, the images are not distorted towards the edges, as it happens when a wide angle lens is used. With the above specifications and placing the camera at a distance of 400 mm from the sample, the images collected cover a window of about 120 mm $\times$ 80 mm. Each image is stored as a gray scale *tiff* picture: dark areas are represented by pixels of value close to 0 (black) and the brighter ones by values close to $2^{bit} - 1$ (white).

For a given light signal, the image produced and stored depends on few controlling parameters:

1. the *exposure time* τ, defined as the time during which the camera shutter stays open letting the collected light to reach the CCD sensor;
2. the *lens aperture*, which defines the amount of light passing through the objective;
3. analog *gain* in dB, an analogical amplification of the signal produced by each pixel (in principle only for the signal not for the noise);
4. the *binning* parameter, having possible values between 1 and 5, representing the linear number of pixels over which the signal is evaluated: instead of assigning to each pixel a value, it is possible to assemble squared groups of 4, 9, 16 or 25 pixels whose value will be summed up and assigned to a coarse grained pixel.

The parameters used in these experiments include an exposure time of $\tau = 1$ s, the maximum lens aperture, an analog gain of 35.5 (maximum possible) and a binning of 3, obtaining acquired image as matrices of 1412 $\times$ 942 pixels and aperture fixed to the value of 2.1 corresponding to the maximum aperture possible. We saved every image as 8-bits, which means that every pixel has a value ranging from 0 (black) and $2^8 - 1 = 255$ (white). The choice of the pixel depth (bit value) is a trade off between memory used and image details: since the camera noise is about 1 % of the maximum value (white), using bit > 8 results in images occupying larger space on the computer, without carrying any information distinguishable from numerical noise. Each image pixel has a linear size of about 100 μm (spatial resolution). Before the beginning of each experiment, the optic is focused on the mid-depth of the flow cell (described below).

2.2 Conservative tracer

To measure the mixing front kinematics of the conservative displacement between two solutions, it is necessary to measure the temporal evolution of the spatial distribution of the concentration field of the invading, or the defending, transported substance. We consider water as defending fluid that will be displaced by a water solution of fluorescein sodium salt, a powder soluble in water that is widely used as a fluorescent tracer for many laboratory and field applications. Fluorescein absorbs light around 494 nm, get in an electronic excited state that instantaneously decay and emits light around 521 nm (in water). These two wave lengths, for excitation and emission respectively, are achieved using a cutter filter (between the panel light and the cell) which locks wave lengths above 500 nm, and a band-pass filter (located between the cell and the camera) which allows only the emitted wave length to reach the camera.

2.3 Chemiluminescent reaction

The considered chemical reaction is luminol ($C_8H_7N_2O_2$, 177.16 g/mol) oxidation by potassium permanganate ($KMnO_4$, 158.9 g/mol). Luminol is a widely used chemiluminescent reactant and the chemiluminescent reaction between luminol and potassium permanganate has been employed to determine concentration

of pharmaceutical or organic molecules in water, blood or urine ([47, 48, 49]). The two reactants are dissolved in aqueous solution (we used milliQ water); NaOH is added to a prepared luminol solution to increase the pH up to 12 resulting in a faster kinetics. More in detail, we first add NaOH to the luminol solution so that OH^- reacts with luminol to produce a luminol dianion, which will be oxidized by $KMnO_4$ to produce a 3-aminophalate in excited state that collapses back to the stable state emitting a single photon. The procedure followed for the two solutions is a modified version of [47]. For simplicity we will indicate with c_A the concentration of luminol and with c_B the potassium permanganate concentration. Figure 8 gives an example (for four time steps) of the light produced when a solution of A is injected in a B saturated porous medium: the reaction takes place at the interface of A and B and we can see the bright field at the front of the plume where injected A encounters fresh B solution and shaded field at the back of the plume where B is depleted. The reaction kinetics is tested and measured for different concentrations of the two reactants. [49] indicates

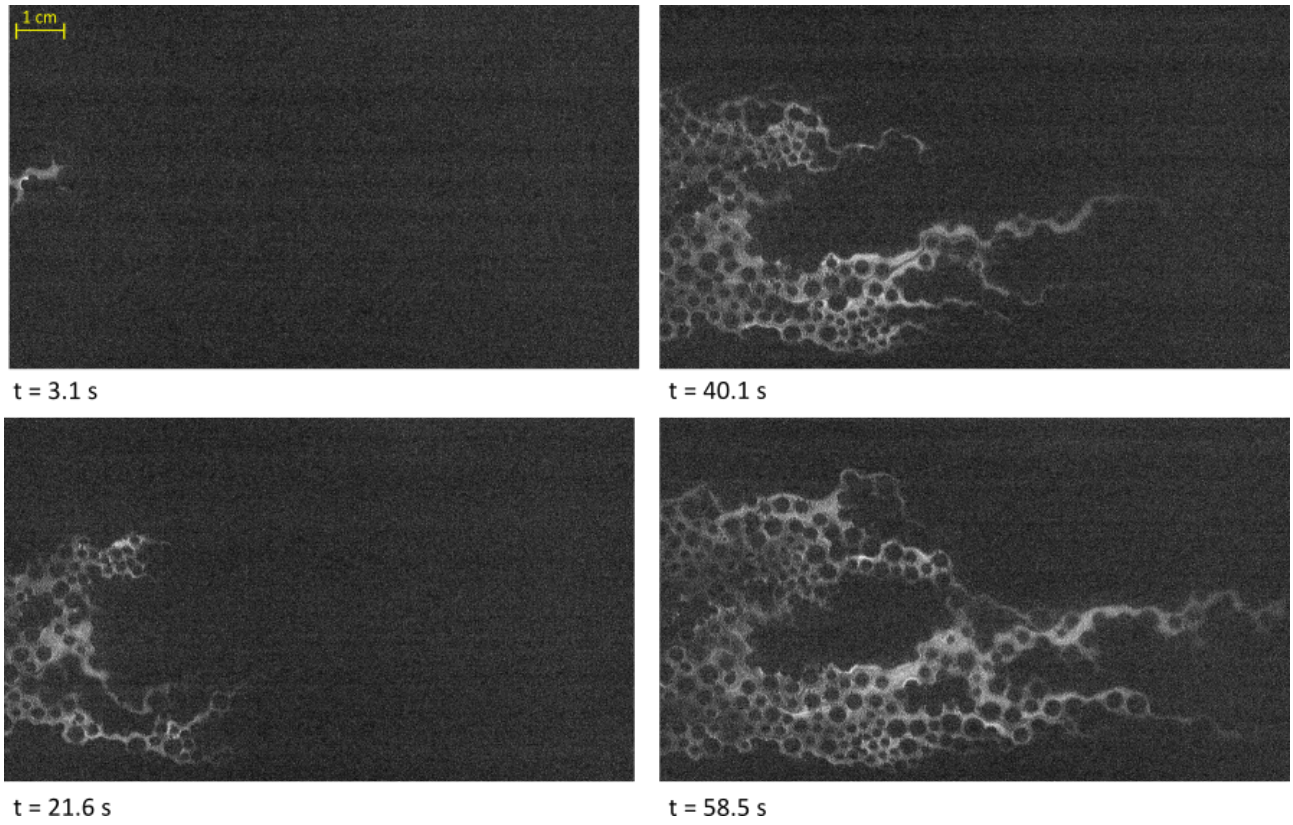

Figure 8: Light intensity field of reactive front of A (luminol) invading B ($KMnO_4$) at four time steps; water saturation w_3=0.93 and flow rate of Q_3=0.03 ml/s.

that intensity of the chemiluminescent reaction increases with increasing luminol concentration. However we cannot tune much A initial concentration due to its low solubility in water. We dissolved 1.76 g of A in 1 L of water, serving as a base A solution of 10 mM and we worked by increasing the concentration of the B solution. Given an initial A concentration c_{A0}, the light produced by the reaction taking place in a perfect mixture increases with the initial B concentration c_{B0}. Different B solutions were prepared from a 0.2 M stock solution and tested with the A base solution. We observed that higher B concentration result in the formation of solid precipitate. Finally, solutions of A 10 mM and B 3 mM are choose as optimal concentrations.

2.4 Flow cell and injection system

The remotely controlled camera is fixed to an aluminum structure build on top of a flow cell within which fluids are injected and mixed using a pump system, as described below.

2.4.1 The porous medium replica

The flow cell is a silicone model of a 2D porous medium enclosed between two Plexiglas plates (Figure 9). The porous medium geometry is first engraved in a Plexiglas plate to obtain a mold, which is then filled with silicone to form the model. Silicone used here is PDMS prepared from the *Sylgard* kit (*Dow Croning*) which contains an elastomer base and a curing agent. The curing agent solidifies the elastomer through an organometallic cross-linking reaction. To do so, the elastomer base is mixed 15:1 with the curing agent (decreasing the ratio, like 10:1, will produce a harder PDMS, enhancing the risk of producing little fractures at pipes connections, see below), this liquid mixture is, then, de-gasified in a vacuum chamber (desiccator) for 30 min and poured into the plastic mold: once filled, the mold is placed in an oven at 60 deg C for $\sim$12 h to accelerate the reaction between elastomer and curing agent. The cured PDMS is optically clear, hydrophobic and non- toxic. Finally a porous medium model of dimensions $7\times22\times0.2$ cm is obtained. The model is pinched with 3 holes of 1.25 mm of diameter at the inlet, and 1 hole (of same size) at the outlet to allow tubing connection, as show in Figure 10.

To ensure saturation (i.e. refilling the cell with water and no air trapped) of the porous medium, the cell is assembled under water and the tubing are filled with water before being connected to the cell. For the unsaturated experiments, the cell is assembled in the same way and bubbles are added afterwards by injecting air into it.

2.4.2 The fluids injection to form a sharp front

The invading front is created by suction of a solution A in the cell filled by a solution B. The two solutions are originally in independent reservoirs and get mixed in the flow cell. The front between the two solutions get displaced by the fluid flow and get homogenized (the solutions are mixed) by molecular diffusion. To obtain an initially sharp front, it is necessary that the injected solution A is as pure as possible and not already mixed with the defending one, B. In fact, during the cell saturation with B some of the solution enters into the A inlet and tubing by diffusion: to clean this area, an additional tubing for recirculation between the injection points for A and B is realized (hole (II) in Figure 10). This extra outlet located between the two inlets allows to pump some A (that goes right to the waste without invading the porous medium) and thus clean the A tubing. The flow is imposed with a syringe pump (*Harvard apparatus PHD ULTRA*) connected via a 3- way valve to the outlet hole (IV) and the outlet (II).

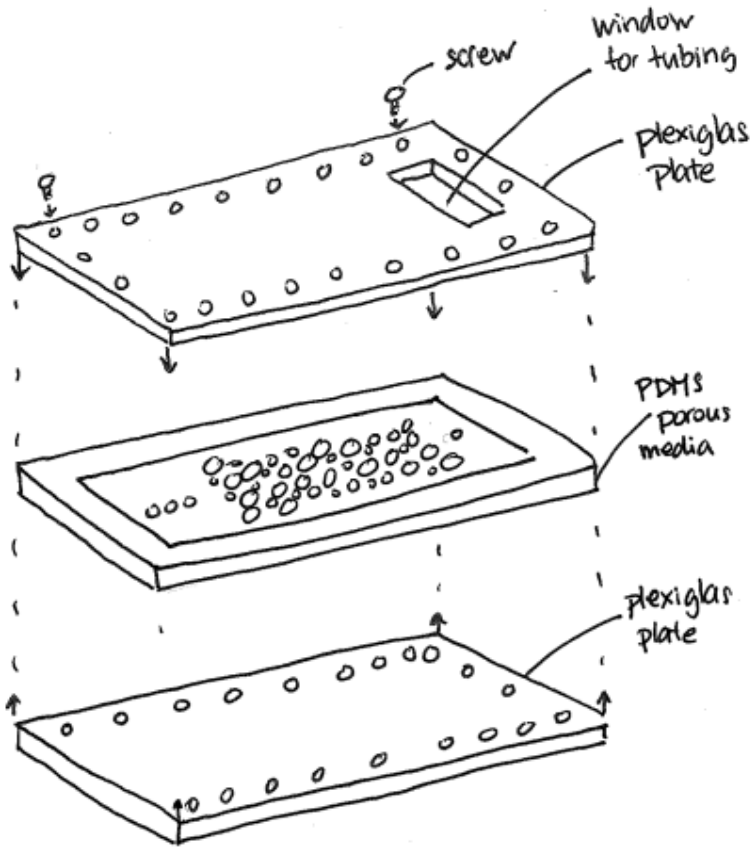

Figure 9: A schematic of a PDMS replica of a porous medium, enclosed between two Plexiglas plate to form the flow cell, which is tightened with steel screws. The model is pinched with 1.25 mm holes to allow tubing connection.

In this way, we ensure that the front between the injected solutions is as sharp as possible. In practice, the injection procedure is performed as follows:

- filling the cell with the reactant B (the B valve is open, the A valve is closed, the pump withdraws from (IV));
- cleaning the injection zone and preparing a sharp interface between the defending B and the A solutions (the B valve is closed, the A valve is open and the pump withdraws from the outlet (II));
- the injection of A in the porous medium begins (the 3-way valve is switched and the pump withdraws from outlet IV).

Therefore, on the one hand of the cell, there are three holes, while on the other hand, only one hole is pinched. Figure 8 shows an example of the sharp front we obtained using the described set-up and procedure.

Two types of flow experiments are performed: the conservative displacement of a water (B) by a water solution of fluorescein (A) and the reactive front between the described solution of potassium permanganate (B) by a luminol solution (A). Conservative and reactive experiments for different water saturation degrees are performed at four different flow rates: Q_1=0.005 ml/s, Q_2=0.01 ml/s, Q_3=0.03 ml/s and Q_2=0.09 ml/s.

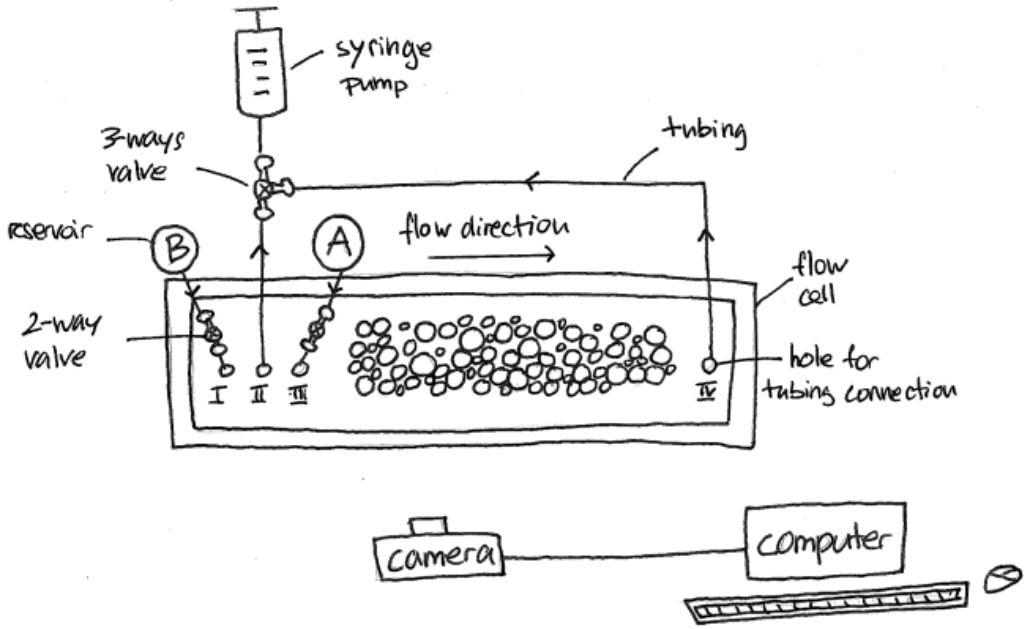

Figure 10: Experimental set-up. Flow is generated by suction using a syringe pump; the porous medium is connected to the reactant reservoirs and the pump through 2 holes via a 3-way valve. (I) is the B ($KMnO_4$) inlet, (III) the A (luminol) inlet, (II) the cleaning outlet, and (IV) is the main outlet. The arrows indicate the flow direction in the pipes.

2.5 Image processing

For both types of experiments, reactive (global reaction kinetics) and conservative (front elongation and stretching), each time series of recorded images is converted into a matrix of real (double floating) values and it is processed as described below. A sample of time series of recorded images is presented in Figure 12 (vessel experiment) and Figure 8. The quantitative image analysis is carried out with a MATLAB code written ad hoc.

2.5.1 The mask

First, it is of primary importance to remove from the quantitative analysis the pixels belonging to the solid immobile grains, in order to be sure to observe only the front reactivity and mixing. This is done by multiplying each image to a binary matrix which has values of one in each pixel corresponding to a pore and zeros for grains. Moreover, from the grains position we measure the porosity and saturation of the porous medium. To do that, a bright picture is taken at the beginning of each experiment (Figure 11.a). From this picture, a binary image, a mask, with value one for each pixel belonging to a pore and zero for each pixel in a grain, is defined (Figure 11.b).

From the same initial picture we also differentiate between the pixels covered by water and those covered by air (Figure 11.c). We now compute: *i*) the total surface of the cell S_{cell} as the total area of the mask (total number of pixel in the picture), *ii*) the total surface of the pores $S_{pores} = \sum_{i,j} mask(i,j)$, and *iii*) the total surface occupied by water S_{water}. Then, the porosity is defined as $n = S_{pores}/S_{cell}$; and the saturation is

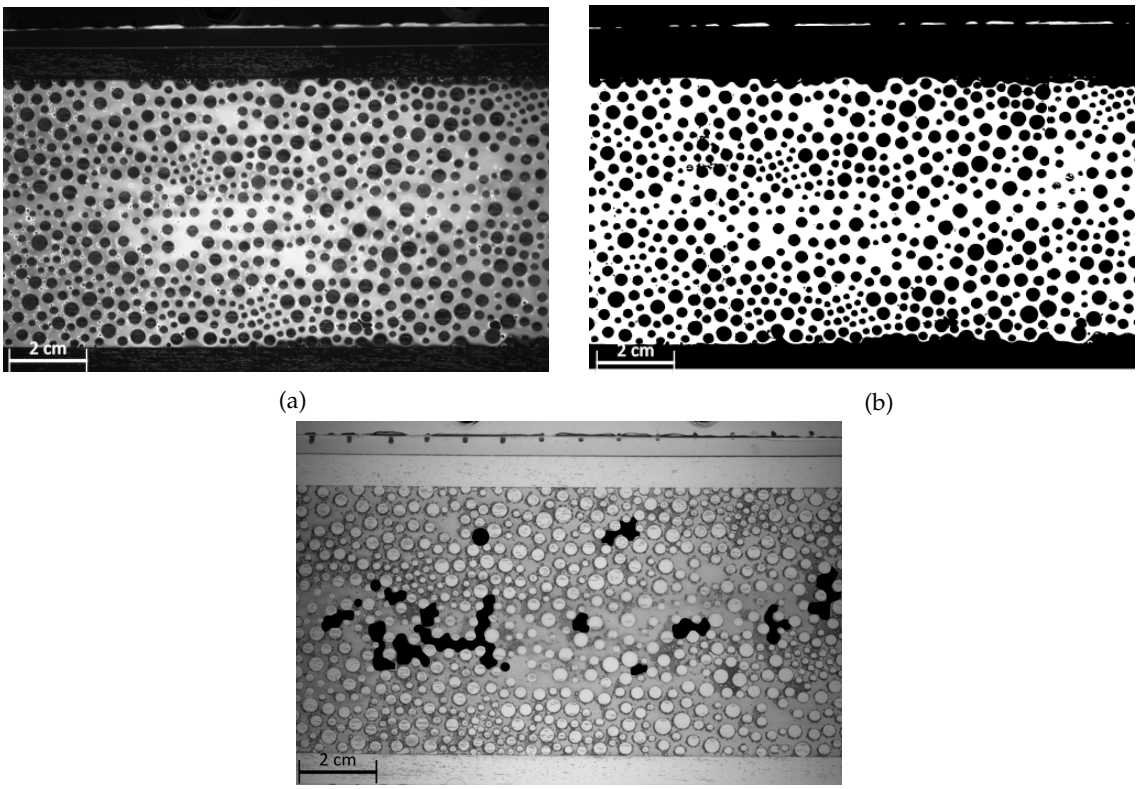

(a) (b)

(c)

Figure 11: a) Initial picture of the porous media. b) Mask used to compute porosity, pore size, and pore throat. c) Mask used to compute saturation: black surface correspond to air bubbles.

defined as $w = S_{water}/S_{pore}$; the average pore size is approximates as $\lambda = S_{pores}/n_{pores}$; and the pore throat is approximate by $h = \lambda/4$. Table 1 lists those properties for the porous medium used here.

n [-]	λ [mm]	h [mm]	w_2 [-]	w_3 [-]	w_4 [-]
0.64	7.9	2	0.96	0.93	0.87

Table 1: Porous medium properties: n is porosity, λ is pore size, h is pore throat, w is saturation degree. w_1=1 is the saturated case.

2.5.2 The conservative front kinematics

The front between two miscible solutions evolves due to advection, that deforms and stretches the front along the local direction of flow and molecular diffusion, that dissipates the local gradients by mixing the two solutions A and B. Therefore, a displacing miscible front is the blurred interface separating the zone fully saturated in A and the zone fully saturated in B. We, thus, define the front location as the position of the local maximum of the invading concentration gradient. If in the two solutions the tracer has the same diffusivity, we can assume that the local maximum of the gradients is located at the isoconcentration lines $c = c_0/2$, where c_0 is the injected concentration value. This will simplify the image processing avoiding the mathematical problem of locating the local maximum of a field, replacing it with the much simpler thresholding problem.

The concentration field of the invading fluorescent tracer could be evaluated via a calibration procedure from the detected light intensity emitted by the moving tracer. The calibration is necessary because the fluorescein is not fully transparent, but slightly colored (when not too diluted), this means that it blocks some of the light produced by the fluorescent tracer, reducing the light detected at higher concentrations. Due to time constraints, the calibration procedure is not done in the framework of this master project, therefore, we simply use the light intensity detected as it was proportional to the concentration field of the tracer. Being aware of this important approximation, we proceed as follows.

At each time t, the reaction kinetics is quantified in terms of the sum of light intensity over the image taken at time t, as $I(t) = \sum_{i,j} p(i,j,t)$. Images are processed through the following steps:

1. in a loop over the number of all recorded pictures, each image is loaded, converted into a matrix of double floating numbers and divided by the bit depth (here 8-bits, thus, by 255) to have the light intensity values normalized between 0 and 1;

2. to remove the camera electronic noise a Gaussian filter is applied over a 3×3 window (basically, pixel values over that window are averaged);

3. to remove the background noise associated to the fact that the image of pure water is not completely black, the first image is set as background, from it a threshold is defined as $tr = 1.2\times$ the average background value, then for each image all pixels whose value is lower than that threshold are set to zero.

Now the tracer concentration is ranging between 0 and 1. We locate coordinates of each point in this processed image whose value is 1/2: in practice we set to zero every pixel with value below 1/2 and to 1 every pixel above 1/2: using the MATLAB function *bwboundaries* we determine the location (x_i, y_i) of each point at the boundary between these black (0) and white (1) zones. The length of the front is then defined as the sum of the Euclidean distance between each points:

$$\Sigma(t) = \sum_{i=2}^{N} \sqrt{(x_{i+1} - x_i)^2 + (y_{i+1} - y_i)^2} \tag{15}$$

where N is the number of points composing the front in the image taken at time t.

2.6 Kinetics of the reaction in well mixed conditions

As discussed in the introduction, the kinetics of a reaction among diluted and well mixed reactants is described by the mass action law: it is proportional to the product of the involved concentration elevated to the power of their stoichiometric coefficient. Here we consider an irreversible bimolecular reaction between two reactants A and B whose initial concentration is $c_{B0} \gg c_{A0}$: therefore, the chemical B concentration is not going to be affected by the reaction, while the one of A will be depleted exponentially fast as described by Eq.12 (Section 1.4.1). The kinetics of such a reaction is measured by taking pictures of a vessel originally filled with A, while B is quickly injected and mixed. We, then, define the reaction rate at time t as proportional to the total amount of light detected by the camera during its exposure time. Figure 12 presents a sample of the images obtained; we can see the light intensity decreasing from time $t = 0$ s when the two chemicals are mixed to the almost black image at $t = 96$ s.

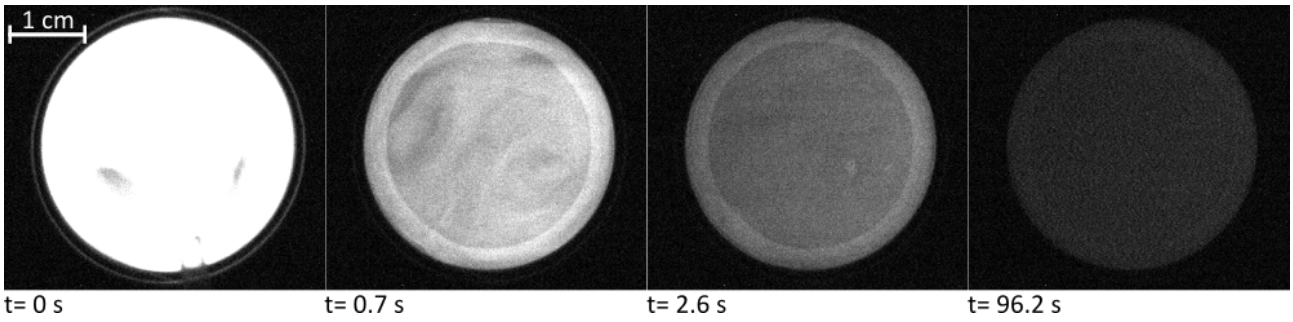

Figure 12: Reaction produced by mixing A and B in a glass vessel; light detected by the camera during an exposure of 200 ms at four time steps.

The total amount of light I_R produced by the reaction during the camera exposure time τ is equal to the consumption of A, thus:

$$I_R = \frac{dc_A}{dt} = -k' c_{A0}\, e^{-k' t}. \tag{16}$$

For each image recorded, we define the total amount of light I_R as the summation of pixel values over all the given image.

2.7 Kinetics of the displacing reaction front

From each of the images of the invading reactive front, we measure the overall reaction kinetics as proportional to the sum of all the image pixel values, after the following processing.

1. Within a loop over the number of all recorded pictures, each image is loaded, converted into a matrix of double floating numbers and divided by the bit depth (here 8-bits, thus, by 255) to have the light intensity values normalized between 0 and 1;
2. to remove the camera electronic noise a Gaussian filter is applied over a 3×3 window (basically, pixel values over that window are averaged);

3. to remove the background noise associated to the fact that pixels associated to zones where no reaction is taking place are not completely black (not exactly 0), the first image is set as background. From it a threshold is defined as $tr = 1.2\times$ the average background value, then for each image all pixels whose value is lower than that threshold are set to zero.

The results of the data analysis is described in the next section.

3 Results

3.1 Kinetics of the reaction

As mentioned in Section 2.6, the kinetics of the reaction in well-mixed conditions is measured by quickly mixing 1 ml of A with 1 ml of B in a glass vessel. The size of the vessel and the volume of reactants are such that the thickness of the reacting solutions layer is similar to the one we have in the flow cell, ~ 2 mm. This gives, also, an estimation of the maximum intensity produced by the reaction in such a volume, allowing us to properly configure camera and optics parameters. The images acquired during this experiment are presented in Figure 12 (Section 2.6) for four time steps.

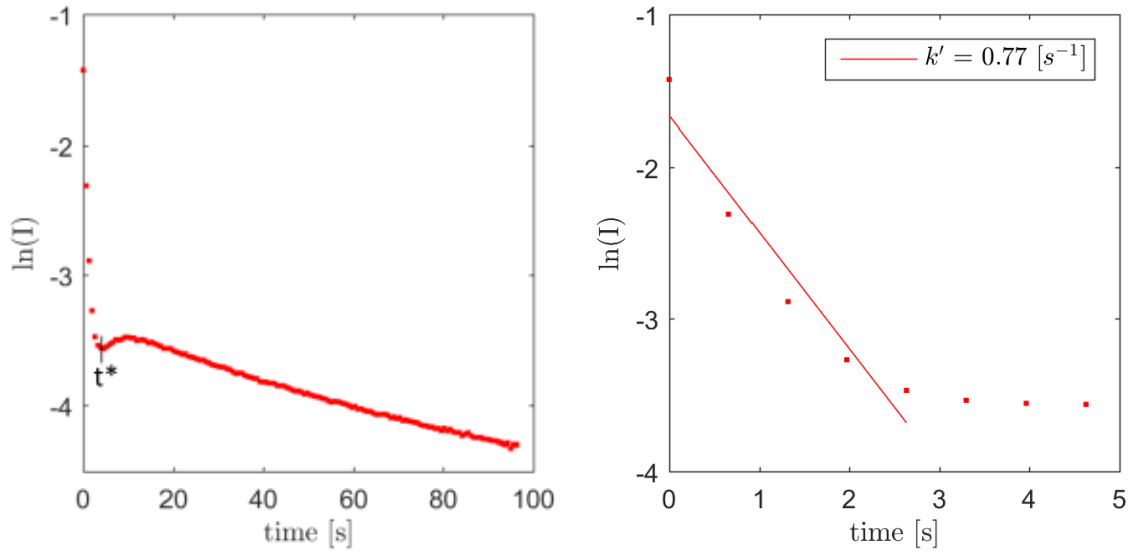

Figure 13: a) Light intensity as function of time in a well mixed experiment for a pseudo first order reaction; two regimes are visible: a first fast drop of light intensity for the reactants that are well-mixed and then a slower drop, this is due to incomplete mixing of the whole solution and thus some of the chemicals react with a lag (mixing limited reaction). b) The first regime is representative of the kinetics of the reaction in well-mixed conditions, so reaction rate k [s^{-1}] is computed as the slope of the intensity decrease of the first five data points.

Figure 13 shows the light intensity observed by the camera as function of time, the data are displayed in semi-log scale to highlight the exponential nature of these kinetics. Until $t^* \sim 2.6$ s (Fig13.a), the light intensity decreases by a factor ~ 10 due to fast mixing caused by injection of the chemicals in the vessel. At $t > t^*$ light is still produced but drops at a much slower rate. We argue that initially the two chemicals are well mixed by the turbulence originated by their abrupt stirring, for times larger than t^* the average reactants concentration has been depleted and, therefore, the reaction stops. Only further mixing, now controlled by molecular diffusion, allows new reactions to take place, resulting in a slower reaction rate. If this is true, this behavior would be a consequence of the mixing technique used, which does not produce an instantaneous and complete mixing: therefore, we consider that the rate of the considered reaction under well-mixed

conditions is described by the first drop of light intensity, i.e. the data acquired until t^*, where we assume a well-mixed condition. According to Eq.16, we can compute the reaction rate constant of our pseudo first order reaction k' as the slope of the natural log of light intensity I as function of time, the fitting of k' is presented in Figure 13. Here $k' = 0.77$ [s^{-1}].

In the following flow experiments we want to consider a fast reaction with respect to advection, meaning that where the reactant are mixed the reaction happens completely before advection continues the mixing. The Damköhler number D_a (see Section 1.5) measures the ratio between the characteristic time of advection τ_a (time required for the flow to travel a pore size distance) and the characteristic time of reaction τ_r (time required for the reaction rate to decrease of one order of magnitude), $D_a = \tau_a/\tau_r$, with $\tau_a = \lambda/u_f$ and $\tau_r = 1/k'$, where $\lambda = 7.9$ mm is the average pore size and $u_f = Q/A$ the front (Darcy) velocity ($A = 7 \times 0.2$ $cm^2 = 1.4$ cm^2 is the flow cell cross section). The condition for a mixing-limited reaction is $D_a \gg 1$. This condition limits the possible experimental flow rates for a given reaction rate constant k'. Table 2 gives for each experimental flow rate Q_i the value of Damköhler number D_a.

	Q_1	Q_2	Q_3	Q_4
u_f $[\frac{m}{s}]$	$5.6\ 10^{-4}$	$1.1\ 10^{-3}$	$3.3\ 10^{-3}$	10^{-2}
$\boldsymbol{\tau_a}$	141.57	7.08	2.36	0.79
$\boldsymbol{\tau_r}$	1.30	1.30	1.30	1.30
$\boldsymbol{D_a}$	109.01	5.45	1.82	0.61

Table 2: Experimental flow rates (Q_1 = 0.005 ml/s; Q_2 = 0.01 ml/s; Q_3 = 0.03 ml/s; Q_4 = 0.09 ml/s) and corresponding Damköhler numbers.

3.2 Conservative front stretching

During the conservative experiments we measure the light intensity field of fluorescein entering a porous medium (Figure 14). The picture, converted into a matrix of double floating values, is used as a proxy for concentration field of fluorescent tracer. From this matrix we trace the isocontour line $I = 0.5$, which is, as mentioned in Section 2.5.2, an approximation of the set of points of local maximum gradient (Figure 14); this isocontour line defines the reactants front. Figure 14 gives an example of the light detected (in a zoomed region of the porous medium), as well as the front line delimitation computed from the light intensity field.

We compute distance between cells of the isocontour line for each time step as in Eq.15, which provides the front length Σ evolution as function of time. The experiment is carried for the four investigated flow rates (Q_1-Q_4, see Section 2.4.2). Figure 15 shows the values of $\Sigma_i - \Sigma_0$ for each recording time i, where Σ_0 is the initial front length defined as the pore space length normal to the main flow direction (cell width minus the transverse space occupy by the pores).

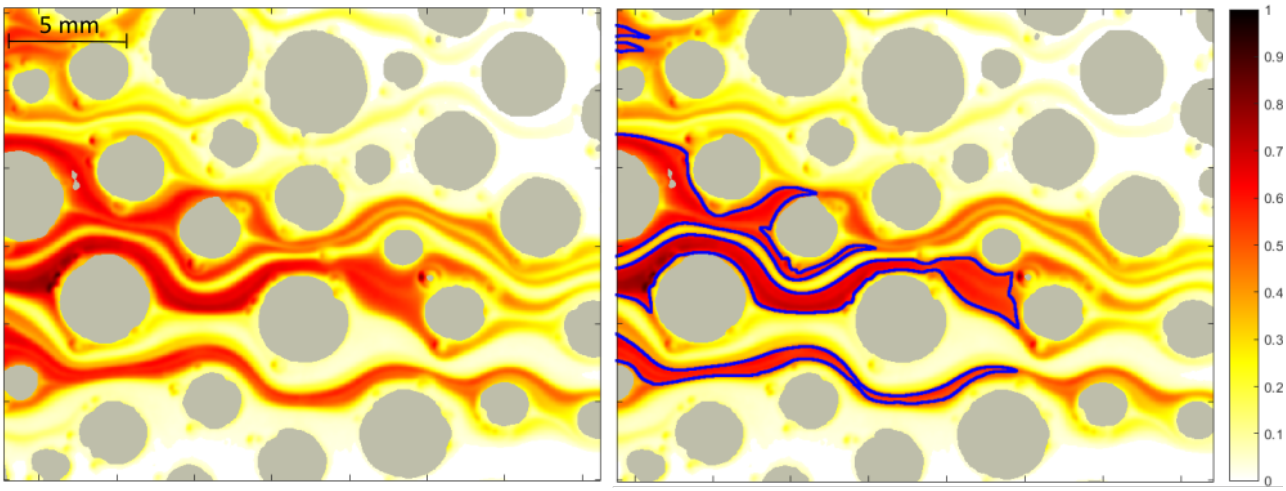

Figure 14: a) Light intensity field I of conservative tracer entering porous media. b) Isocontour line defined where $I = 0.5$. This line is used as a proxy for the front delimitation.

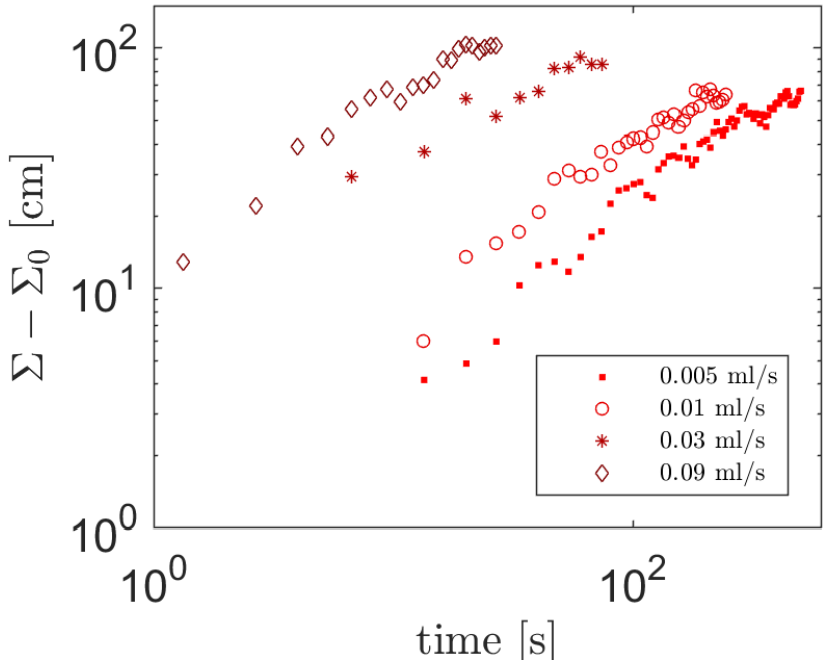

Figure 15: Conservative front stretching: front length evolution, $\Sigma - \Sigma_0$, for the four experimental flow rates.

The data presented in Figure 15 shows that the front length keeps growing with time. This indicates that none of the experiment reached the coalescence regime described by [20], where the lamellae start to overlap and thus the front length decreases. This is consistent with the fact that different fingers are supposed to merge due to diffusion. Coalescence starts when the mixing time is reached: which corresponds to the time required for diffusion to mix solution over the average finger distance. This distance is given by the pore size $h \sim 2$ mm. The mixing time is then defined as $h^2/2D \sim 3000$ s; in this case mixing time is longer than our experimental time and thus coalescence is not reached.

3.3 Heterogeneous flow, reactive front in saturated and unsaturated porous media

The images acquired during the reactive experiments show the field of light intensity produced by the chemiluminescent reaction between A and B. A sample of the collected images is presented in Figure 16 for four experiments (flow rates Q_3 and Q_4, and saturation degrees w_1 and w_4), at different time steps.

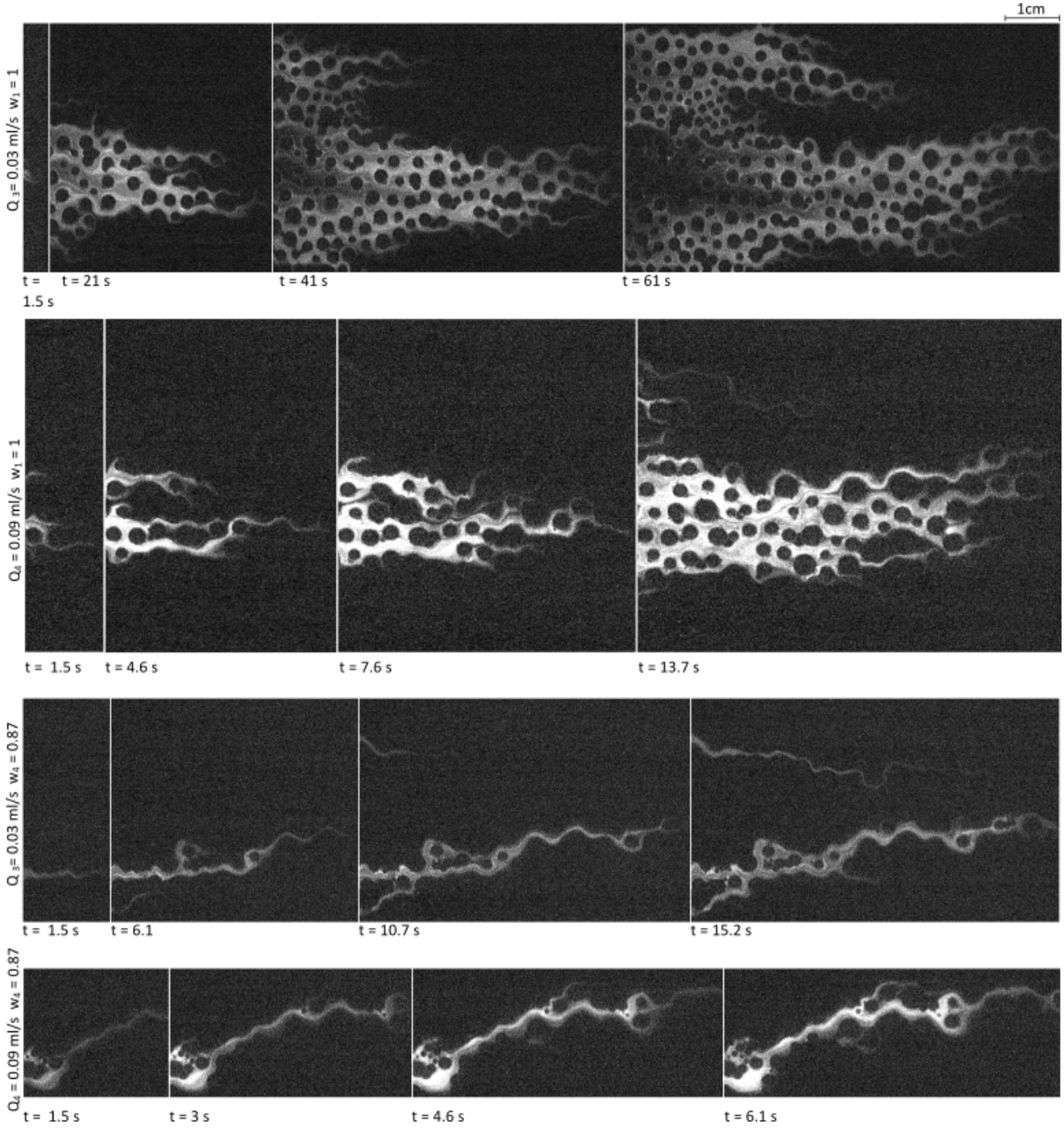

Figure 16: Field of light intensity produced by the oxidation of A (luminol) by B ($KMnO_4$) in four experiments. Q is the flow rate applied and w the saturation in the porous medium. For each data set (row), the first image shows the front as it enters the camera field of view and the last one when it exits it.

First, we can observe that for a given saturation degree the plume is brighter for the highest flow rate, indicating faster reaction rate for faster flow velocity. Secondly, the shape of the plume differs significantly between saturated and unsaturated case even though the saturation degree is similar (w_1=1 and w_4=0.87). Indeed, while the front spreads into several lamellae in the saturated case, in the unsaturated one, high velocity area compress the front in a single finger that crosses camera field of view about twice faster as the saturated front. What we observe here is an increase of the velocity field heterogeneity caused by the presence of air bubbles (see Section 1.6).

As mentioned in Section 2.6, we compute from the collected images the total light intensity I as the sum of pixel value in one image. Figure 17 presents the results for the set of the 16 reactive experiments.

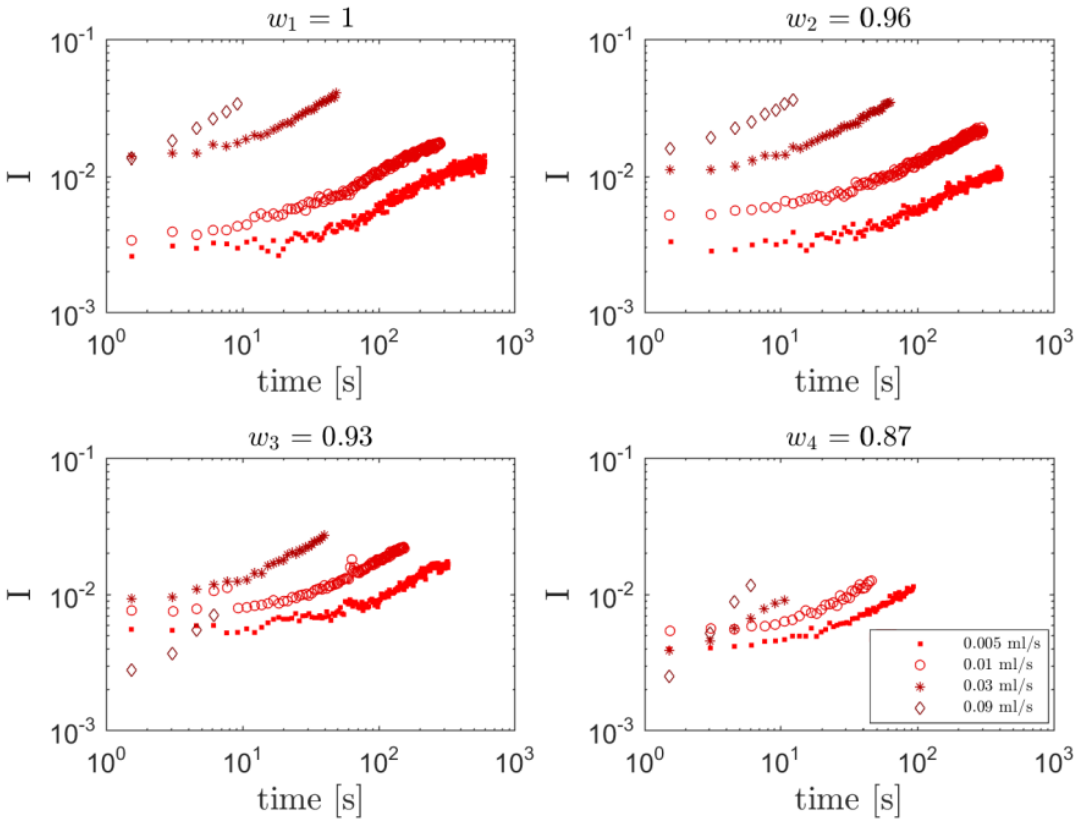

Figure 17: Reactive experiments, light intensity (I) as function of time for different flow rates (symbol) and different saturation degrees w.

In all experiments the total amount of light keeps increasing with time, and for a given saturation degree w the process appears to be driven by advection. Although different saturation shows different results, the main driver is flow rate. These observations are further discussed in the next section.

4 Discussion

4.1 Conservative front stretching

The dynamics of the front geometry (width s and length Σ) is controlled by the competition between stretching and diffusion. The front stretching induces its compression in the direction perpendicular to the local flow and thus reduces the front width. On the other hand, diffusion works in the opposite direction, widening the invading reactant lamellae. Since pure advection conserves the volume of displaced fluid (Σ), the compression of the front width is described by:

$$s\,\frac{d\Sigma}{dt} + \Sigma\,\frac{ds}{dt} = 0 \qquad \frac{1}{s}\,\frac{ds}{dt} = -\frac{1}{\Sigma}\,\frac{d\Sigma}{dt}, \tag{17}$$

while in a purely diffusive case, the average front width grows as:

$$\frac{ds}{dt}\frac{1}{s} = \frac{D}{s^2}. \tag{18}$$

Eq.17 and Eq.18 together give the expression for the front width evolution:

$$\frac{1}{s}\,\frac{ds}{dt} = \frac{D}{s^2} - \frac{1}{\Sigma}\frac{d\Sigma}{dt}. \tag{19}$$

At short times, the front length increases linearly and is given by:

$$\Sigma(t) = \Sigma_0\,(1 + \gamma\,t). \tag{20}$$

where Σ_0 represents the initial front length. Therefore, Eq.19 can be analytically solved, giving the expression for average front width evolution [50]:

$$s(t) = s_0\sqrt{\frac{3\,\beta - 2 + 2\,(1+\gamma\,t)^3}{3\,\beta\,(1+\gamma\,t)^2}}, \tag{21}$$

where $\beta = \frac{s_0^2\,\gamma}{D}$ and s_0 the initial front width.

After a certain time t^*, compression and diffusion start to equilibrate and the growing lamellae will eventually overlap leading to the coalescence of the front. This time is called mixing time $t^* \propto \beta^{1/3}$ [37]. Before mixing time, stretching increases $\Sigma(t)$ as described by Eq.20, and $s(t)$ decreases due to compression. At $t > t^*$, $\Sigma(t)$ do not follow linear growth anymore and $s(t)$ start to increase as$\sqrt{D\,t}$, i.e. diffusion becomes the dominant process.

The results presented in Figure 15 indicate a strong correlation of front length growth rate and the applied flow rate. We can see that the process is dominated by advection: the front length increases at a rate proportional to the flow rate Q, this can be verified by normalizing the data by the applied flow rate (Figure 18 left), collapsing normalized data in one line.

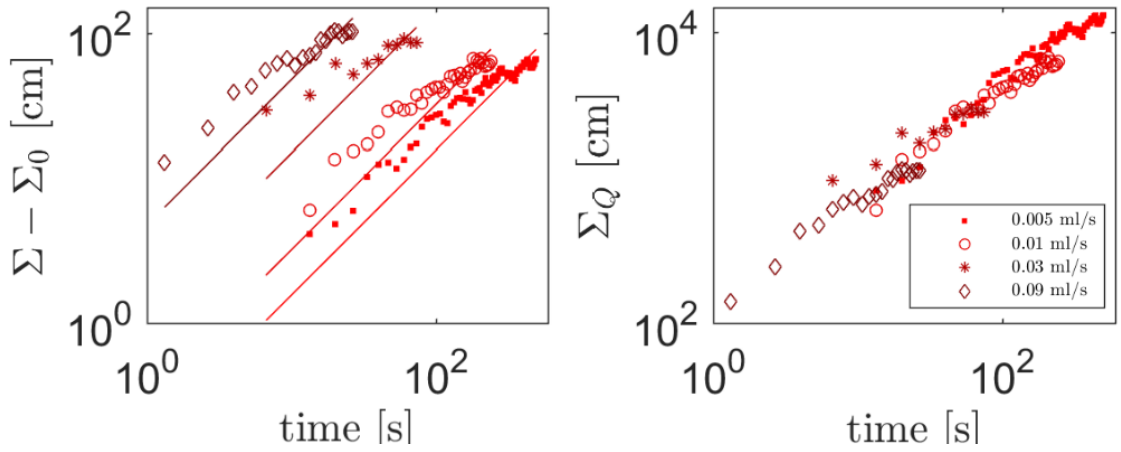

Figure 18: Conservative front stretching: front length evolution, $\Sigma - \Sigma_0$, for the four experimental flow rates. Right: model for linear growth of front length $\Sigma_0\,\gamma_0\,t$ (lines); left: front length data normalized by their respective flow rate $\Sigma_Q = \frac{\Sigma - \Sigma_0}{Q}$.

The data are well fitted (Figure 18) by the growth model presented in Eq.20, where front length evolves linearly with time and proportionally to a stretching coefficient γ. Here $\Sigma - \Sigma_0$ is fitted to the model $\Sigma_0\,\gamma_0\,t$ to define γ_0 for each flow rate. Table 3 summarizes the values of the stretching rate γ_0 fitted for the four flow rates. Since the observed front length growth is proportional to the applied flow rate, given a value γ_0 for a

	Q_1	Q_2	Q_3	Q_4
γ_0	0.03	0.06	0.30	0.95

Table 3: Stretching rate γ_0 fitted to the front length evolution measured in conservative experiments. Q_i are the applied flow rates in [ml/s].

certain flow rate Q_0, the stretching rate at flow rate Q is given by [20]:

$$\gamma = \gamma_0 \frac{Q}{Q_0} \tag{22}$$

The relationship of Eq.22 can be applied to the fitted γ_0 values of the conservative experiment to evaluate the stability of computed stretching rate with respect to the measured one (Table 4). We can see that in general

	Q_1	Q_2	Q_3	Q_4
$Q_0, 1$	**0.03**	0.06	0.19	0.56
$Q_0, 2$	0.03	**0.06**	0.19	0.57
$Q_0, 3$	0.05	0.10	**0.30**	0.89
$Q_0, 4$	0.05	0.10	0.32	**0.95**
σ^2	10^{-4}	$5\ 10^{-4}$	$5\ 10^{-3}$	$4\ 10^{-2}$

Table 4: Experimental and computed stretching rates γ. Q_0 corresponds to the experimental flow rate. For each line the experimental value γ_0 is in bold.

the variance σ^2 for γ values is low, and for a given Q, computed values are similar to measured ones.

4.2 Reactive front in saturated and unsaturated porous media

From the acquired images (Figure 16), we want to study the impact of flow heterogeneity on the consumption of B and thus the production of I. This can be described by the variation of total light intensity I as function of time:

$$I(t) = \int_V c_I(x,t)dx \tag{23}$$

where V the volume of the porous medium, and c the light intensity field in the main flow direction (i.e. x).

In the case where reactants are well mixed within pores, the production of I follows the kinetic described by Eq.16. The solute concentration field is expressed as average concentration over a volume larger than the pore size and the solute transport is considered one dimensional in the flow direction. Then as mentioned in Section 1.5 the temporal evolution of solute concentration is described by the advection-dispersion-reaction equation [37]:

$$n\,\frac{\partial C_I(x,t)}{\partial t} + q\,\frac{\partial C_I(x,t)}{\partial x} - n\,D^*\,\frac{\partial^2 C_I(x,t)}{\partial x^2} = -k' c_I \tag{24}$$

where n is the porosity and D^* is the sum of molecular diffusion and hydrodynamic dispersion. In that case, the temporal evolution of mass of C (product of the reaction between A and B, see Section 1.5) is given by [20]:

$$M_C(t) = c_0\sqrt{\frac{4\,D^*\,t}{\pi}}. \tag{25}$$

The consumption of reactants ($\frac{dM_c}{dt}$) in these systems is fully controlled by D^* and grows as$\sqrt{t}$.

The heterogeneous velocity field existing in porous media creates high and flow velocity areas, which results in a stretching of the concentration field in the flow direction: the front is no more flat but presents a lamella-like topology with fingers of reactant A invading the field of B. The front length is stretched and thus increases the area where concentration gradient is strong, i.e. the area for diffusive mass transfer. The production of C evolves faster than the$\sqrt{t}$ described in Eq.25, and depends on the dynamics of the front length [20]:

$$\frac{dM_C(t)}{dt} = I(t) = D\int_\Gamma |\bigtriangledown c_A|\,d\Sigma \approx D\,\frac{c_0}{s(t)}\,\Sigma_0\,(1+\gamma\,t) \tag{26}$$

where $\frac{c_0}{s(t)}$ is the average concentration gradient over front width and $\Sigma_0\,(1+\gamma\,t)$ is the front length given by the linear growth expressed in Eq.20.

The results of the reactive front experiments are well fitted to the relation described by Eq.26 (Figure 19). The stretching rate γ_0 is the one fitted for flow rate Q_3 of the conservative experiment (Table 4). The other stretching rates γ are derived using Eq.27 where γ_0 is multiplied by the ratio between Q_0 and Q, and additionally to take into account unsaturated conditions, we multiplied γ_0 by the inverse of saturation degree w.

$$\gamma = \gamma_0 \frac{Q}{Q_0} \frac{1}{w} \tag{27}$$

Σ_0 is computed as explained in Section 3.2, and the fitting parameters are s_0 and c_0, initial front width and initial concentration, respectively. The statistics of parameters s_0 and c_0 values are presented in Table 5.

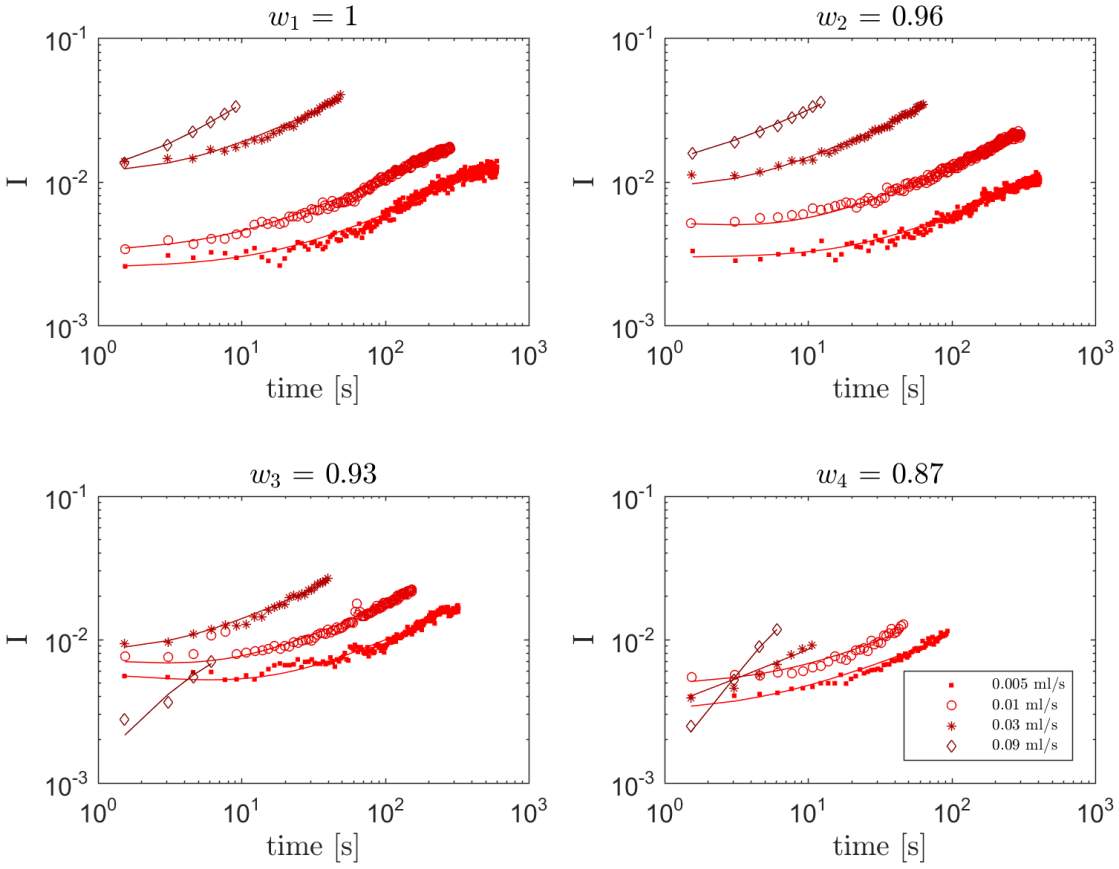

Figure 19: Light intensity I from reactive experiments as function of time for different flow rates (symbol) and different saturation degrees w. Fitting lines of the model $I = D\,\Sigma_0\,c_0\,\frac{1+\gamma\,t}{s(t)}$, with s_0 (initial front width) and c_0 (initial concentration) as parameters, are superimposed. The γ values used are: 0.05 for Q_1=0.005 ml/s, 0.1 for Q_2=0.01 ml/s, 0.3 for Q_3=0.03 ml/s and 0.89 for Q_4=0.09 ml/s.

We define the initial picture (for $t = 0$) as the one in which the front is fully entered within the camera field of view. The initial image used for four data set is shown as example in Figure 20. Equation 26 describes the reaction growth due to front deformation, before that, the observed growth in light intensity is only due to the front entering the camera window. This would be an artifact associated to the visualization of the reaction

	min	max	mean	median	variance
s_0 [cm]	0.02	0.85	0.12	0.06	0.04
c_0	0.02	0.12	0.10	0.08	0.01

Table 5: Statistics for the fitted parameters s_0 and c_0.

(we set the camera to start recording before the front enters the field of view) and, thus, the data must be processed to remove these initial pictures. In this work, the definition of the first image is not done in an automatic manner but manually, observing the pictures and determining from that which is the first one, i.e. when the front is fully enclosed in the camera window.

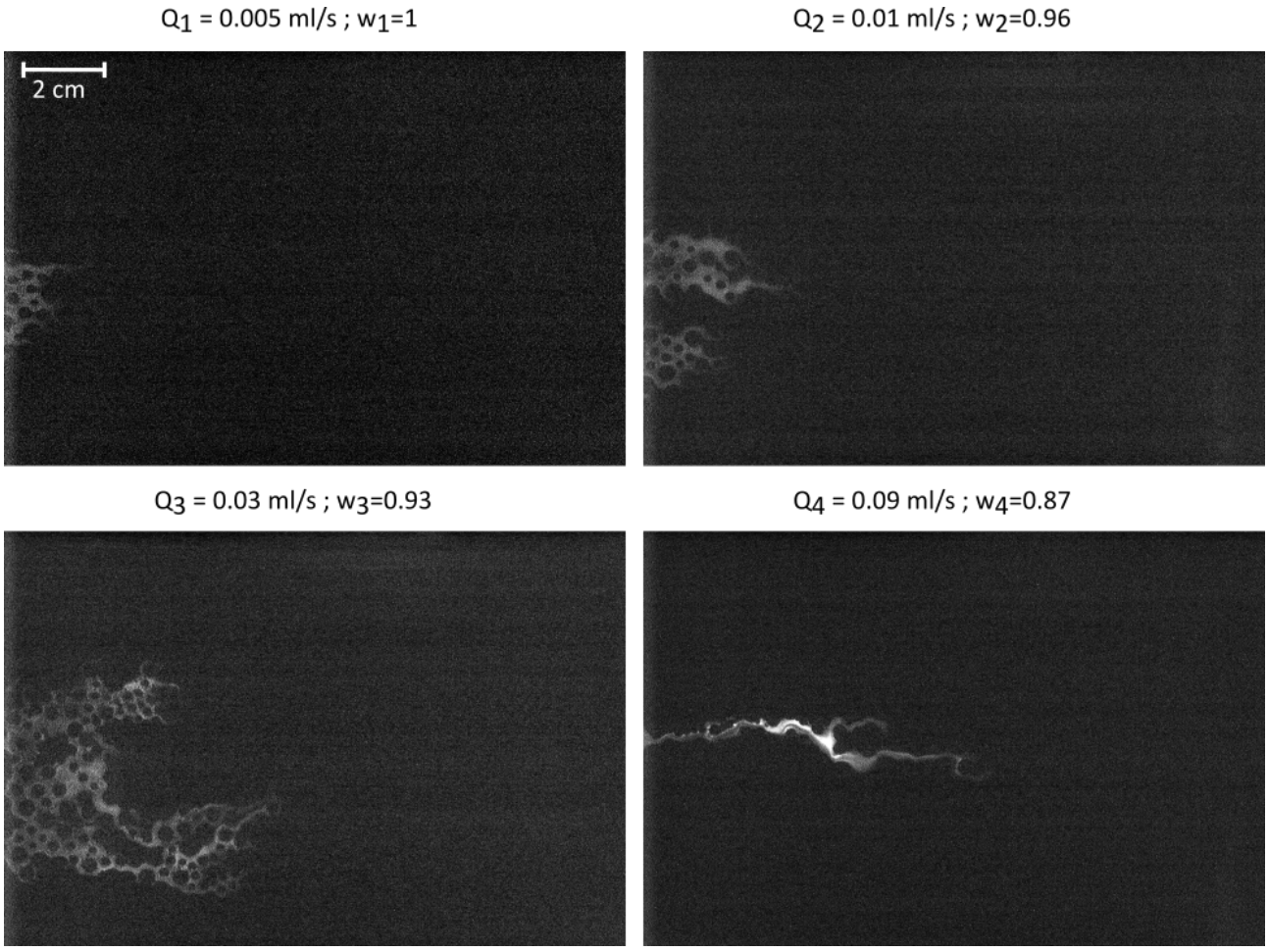

Figure 20: Image used as initial image for four data set. The flow rate is expressed as Q, the saturation degree as w. The front is fully in the camera field of view and from now on the reaction rate evolution can be modeled.

Figure 21 shows the front width evolution, given by Eq.21, for the fitted parameter s_0 and the measured stretching rate γ. We can observe the two regimes described in Section 4.1: at early time advection dominates and diffusion is negligible, therefore the front is compressed due to the elongation of the front, this is called the *stretching regime*, and the front width $s(t)$ decreases approximately as $\frac{1}{t}$; at later time the elongation of the

front is stopped by coalescence of reactant lamellae and diffusion becomes dominant, the front width starts to increase as $\sqrt{D\,t}$, this is called the *dissipation regime*. The point of inflection of the curve $s(t)$ is defined by the *mixing time* $t*$ (see Section 4.1).

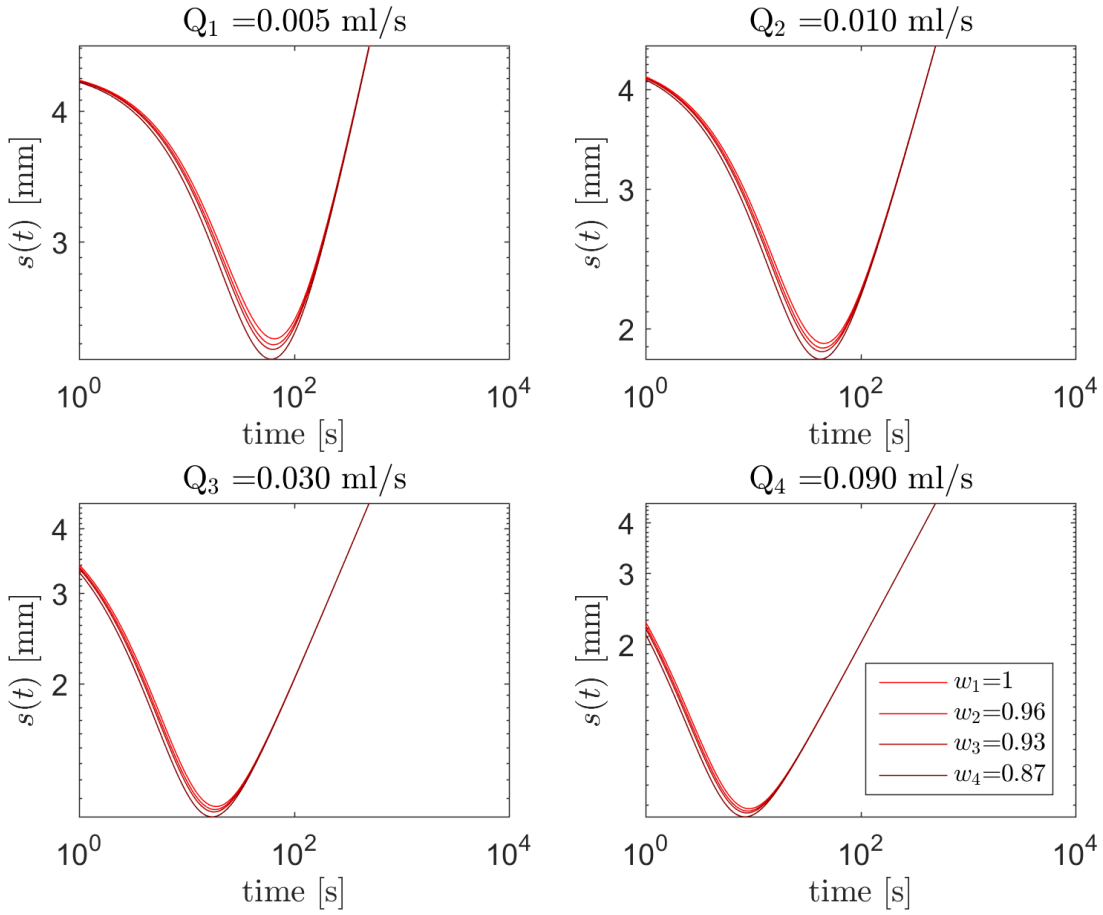

Figure 21: Front width s for the four flow rates and the three saturation degrees studied.

The front length evolution can also be visualized by plotting the expression of front length linear growth describe by Eq.20 using the stretching rate γ fitted from the conservative experiments (Table 4). This is done here for two flow rates (Q_1 and Q_4) and two degrees of saturation (w_1 and w_4), the result is presented in Figure 22.

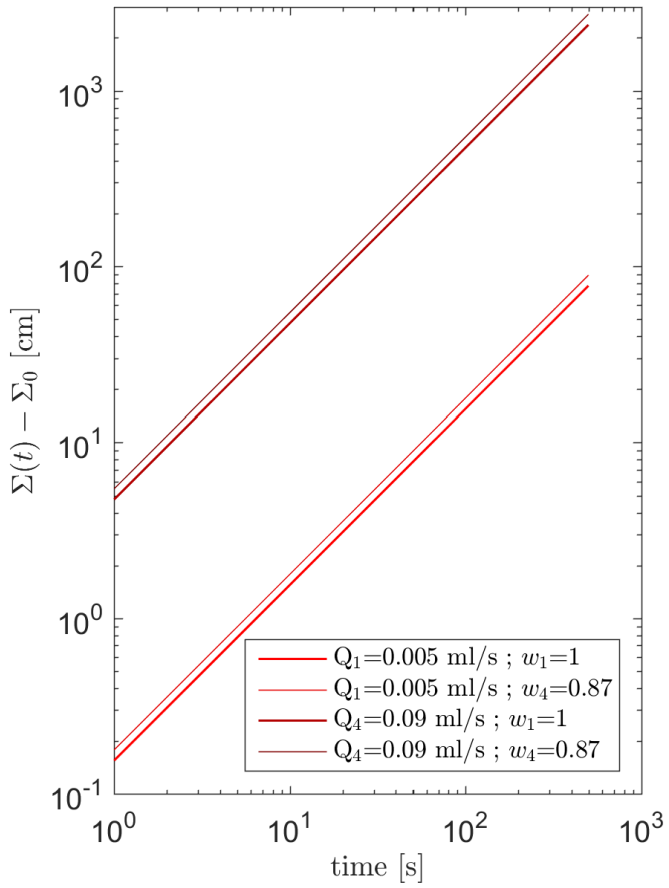

Figure 22: Front length Σ for two flow rates Q and two degrees of saturation w.

In the expression given by Eq.26, the dependence of reaction rate I to flow rate lays in the elongation of the front characterized by the stretching rate γ. As a validation of the expression proposed for γ (Eq.22), we normalize the measured reaction rate by the applied flow rate (Figure 23). We can see that the values of I collapse on the same diagonal, showing that the reaction rate increases proportionally to the applied flow rate and is driven by the front elongation described in Eq.20.

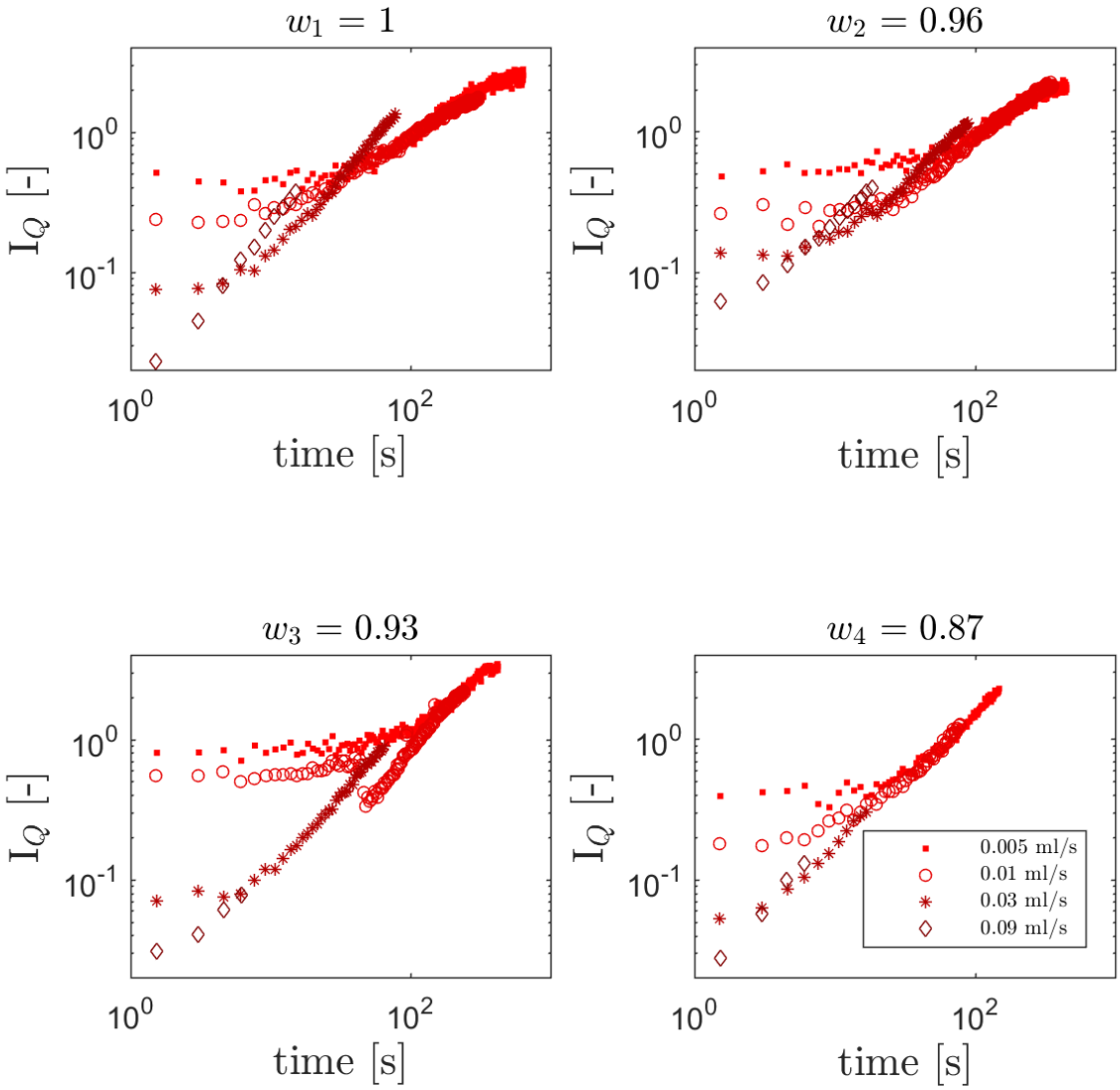

Figure 23: $I_Q = \frac{I}{Q}$: light intensity I normalized by the applied flow rate Q for four saturation degrees w.

Figure 24 shows the same results but grouped by flow rate. For the two low flow rates (Q_1 and Q_2), the reaction rate is higher for the two lower saturation degrees (w_3 and w_4). This illustrates the idea that an increase in heterogeneity, in this case by the presence of air, results in a stronger concentration gradients and thus faster reaction rates (see Section 1.6). On the contrary, for the two higher flow rates (Q_3 and Q_4), the measured reaction rate is lower for the two low saturation degrees. Unfortunately, in the experimental setup used, the camera is fixed and thus we cannot follow the displacement front for long times. At high flow rate and furthermore for decreasing saturation the duration of the experiment is very short and only four data points could be collected. In those conditions it is difficult conclude on the effect of saturation on the reaction rate for high flow rates experiments.

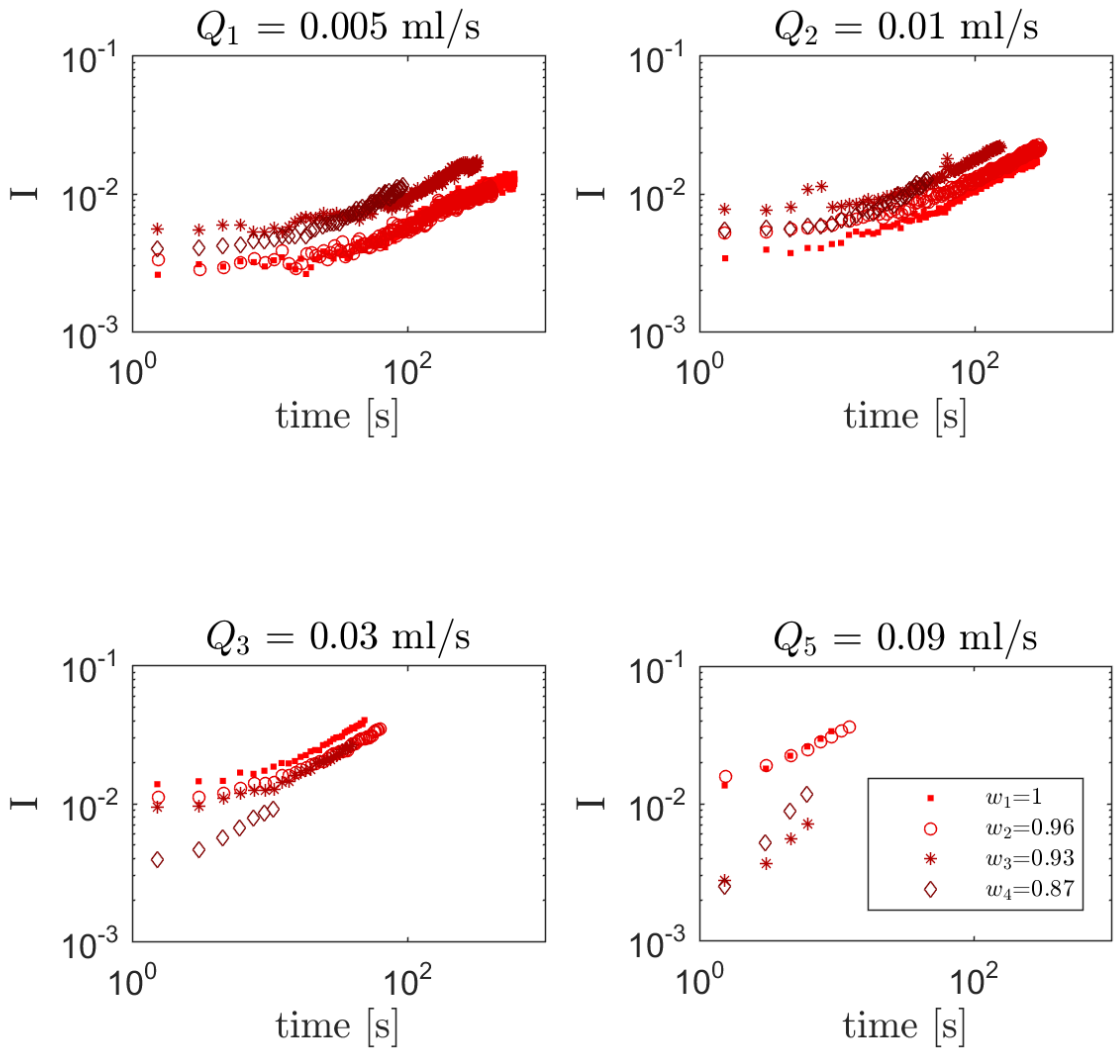

Figure 24: Impact of saturation degree w impact on light intensity I for four flow rates Q.

5 Conclusion

In this work we use an experimental approach to study and characterize mixing and reactive transport in porous media. To do so we visualize the displacement of a front between two solutions in a synthetic porous medium. Description of reactive transport using mass conservation law assumes that there is a scale at which the reactants are well mixed. In classical approach this scale is larger than pore size. However in porous media, grains, and furthermore in the unsaturated case, presence of air bubbles create a heterogeneous velocity field. This heterogeneous velocity field deforms the concentration field into a lamella-like topology which makes spreading due to advection (which tends to increase the concentration gradient) and diffusion (which tends to homogenize the concentration field) happening at different rates. This results in a non-homogeneous solute concentration within pores. To study the impact of this incomplete mixing we perform two types of experiment: one is a conservative flow experiment where we record the displacement of the concentration field of a conservative tracer and measure the front geometry evolution; the second is a reactive flow experiment where we record the displacement of a mixing limited reactive front and measure the reaction rate between the two chemicals. To create a reactive front we optimize a chemiluminescent reaction between luminol and potassium permanganate. The reaction allows the formation of a bright front that is visible by the camera. We produce a sharp front for the saturate case and three unsaturated ones with four flow rates ranging over one order of magnitude. Firstly, we could observe that before coalescence of the lamellae (which was not reached) the front length follows well the linear growth described by [20], furthermore we show that this growth is proportional to the applied flow rate. Secondly, the measured reaction rate recorded during the reactive experiment, is in agreement with the prediction of the model Eq.26 proposed by [20] where the evolution of the front geometry, governed by stretching and molecular diffusion, controls the overall reaction rate. We show that for the four saturation degrees tested, the measured reaction rate is proportional to the flow rate. Additionally for the lowest flow rates we show that the reaction rate is inversely proportional to the saturation degree. For high flow rates our experimental set-up proved to be not adapted and we cannot conclude on the effect of saturation on reaction rate in that case. In the future our experimental set-up should be adapted to study mixing and reactive transport at higher flow rates and lower saturation degree.

References

[1] M. E. McClain, E. W. Boyer, C. L. Dent, S. E. Gergel, N. B. Grimm, P. M. Groffman, S. C. Hart, J. W. Harvey, C. A. Johnston, E. Mayorga, W.H. McDowell, and G. Pinay. Biogeochemical hot spots and hot moments at the interface of terrestrial and aquatic ecosystems. *Ecosystems*, 6:301–312, 2003.

[2] J. Chorover, R. Kretzschmar, F. Garcia-Pichel, and D. L. Sparks. Soil biogeochemical processes within the critical zone. *Elements*, 3(5):321–326, 2007.

[3] P. Grathwohl, H. Rügner, T. Wöhling, K. Osenbrück, M. Schwientek, S. Gayler, U. Wollschläger, B. Selle, M. Pause, J.O. Delfs, M. Grzeschik, U. Weller, M. Ivanov, O. A. Cirpka, U. Maier, B. Kuch, W. Nowak, V. Wulfmeyer, K. Warrach-Sagi, T. Streck, S. Attinger, L. Bilke, P. Dietrich, J. H. Fleckenstein, T. Kalbacher, O. Kolditz, K. Rink, L. Samaniego, H. J. Vogel, U. Werban, and G. Teutsch. Catchments as reactors: a comprehensive approach for water fluxes and solute turnover. *Environ. Earth Sci.*, 69:317–33, 2013.

[4] C.A.J. Appelo and D. Postma. *Geochemistry, groundwater and pollution*. Taylor & Francis 2nd ed., 2005.

[5] P. Serrano-Ortiz, M. Roland, S. Sanchez-Moral, I.A. Janssens, F. Domingo, Y. Goddéris, and A.S. Kowalski. Hidden, abiotic co2 flows and gaseous reservoirs in the terrestrial carbon cycle: review and perspectives. *Agr. Forest. Meteorol.*, (150):321–329, 2010.

[6] G. F. Pinder and M. Celia. *Subsurface hydrology*. Whiley, 2006.

[7] D. Or, B. F. Smets, J. M. Wraith, A. Dechesne, and S. P. Friedman. Physical constraints affecting bacterial habitats and activity in unsaturated porous media - a review. *Adv. Wat. Res.*, 30:1505–1527, 2007.

[8] R. T. Armstrong and D. Wildenschild. Investigating the mechanisms of microbial enhanced oil recovery. *J. Pet. Sci. Eng.*, (94-95):155–163, 2012.

[9] Z. Neufeld and E. Hernandez-Garcia. *Chemical and biological processes in fluid flows: A dynamical system approach*. Imperial College Press, 2010.

[10] T. Tel, A. Demoura, C. Grebogi, and G. Karolyi. Chemical and biological activity in open flows: A dynamical system approach.

[11] W. Horsthemke, S. Fedotov, and V. Mendez. *Reaction-transport systems*. Springer, Berlin, 1st edition, 2010.

[12] M. Dentz, T. Le Borgne, A. Englert, and B. Bijeljic. Mixing, spreading and reaction in heterogeneous media: a brief review. *J. Cont. Hydrol.*, 120–121, 2011.

[13] Stephen B. Pope. *Turbulent flows*. Cambridge University Press, New York, 2000.

[14] J. Bear. *Dynamics of fluids in porous media*. American Elsevier, New York, 1972.

[15] J. Jimenez. Oceanic turbulence at millimeter scales. *Sci. Mar.*, 61, 1997.

[16] J. R. Taylor and R. Stocker. Trade-offs of chemotactic foraging in turbulent water. *Science*, 338, 2012.

[17] P. K. Kang, P. de Anna, J. P. Nunes, B. Bijeljic, M. J. Blunt, and R. Juanes. Pore-scale intermittent velocity structure underpinning anomalous transport through 3-d porous media. *Geophys. Res. Lett.*, GL061475, 2014.

[18] S. S. Datta, H. Chiang, T. S. Ramakrishnan, and D. A. Weitz. Spatial fluctuations of fluid velocities in flow through a three-dimensional porous medium. *Phys. Rev. Lett.*, 111:064501, 2013.

[19] M. Holzner, V. L. Morales, M. Willmann, and M. Dentz. Intermittent Lagrangian velocities and accelerations in three-dimensional porous medium flow. *Phys. Rev. E*, 92:013015, 2015.

[20] P. de Anna, T. Le Borgne, M. Dentz, D. Tartakovsky, A. andBolster, and P. Davy. Flow intermittency, dispersion and correlated continuous time random walks in porous media. *Phys. Rev. Lett.*, 101:184502, 2013.

[21] J. M. Ottino. *The kinematics of mixing: stretching, chaos, and transport*. Cambridge University Press, 1989.

[22] P. K. Kitanidis. The concept of the Dilution Index. *Water Resour. Res.*, 30(7):2011, 1994.

[23] J. Duplat, A. Jouary, and E. Villermaux. Entanglement rules for random mixtures. *Phys. Rev. Lett.*, 105:034504, 2010.

[24] J. Duplat, C. Innocenti, and E. Villermaux. A non-sequential turbulent mixing process. *Phys. Fluids*, 22:035104, 2010.

[25] L. W. Gelhar, C. W. Kenneth, and R. Rehfeldt. A critical review of data on field-scale dispersion in aquifers. *Water Resour. Res.*, 28:1955–1974, 1992.

[26] K. A. Connors. *Chemical kinetics*. VCH publishers, New York, 1990.

[27] P. de Anna, F. Di Patti, D. Fanelli, A. J. McKane, and T. Dauxois. Spatial model of autocatalytic reactions. *Phys. Rev. E*, 81(5), 2010.

[28] C. Lugo and A. McKane. Quasicycles in a spatial predator-prey model. *Phys. Rev. E*, 78(5):1–15, 2008.

[29] F. Schweitzer. *Brownian agents and active particles brownian agents and active particles*. Springer Series in Synergetics, New York, 2003.

[30] S. H. Strogatz. *Non linear dynamics and chaos*. Westview Press, 2000.

[31] C. M. Gramling, C. F. Harvey, and L. C. Meigs. Reactive transport in porous media: A comparison of model prediction with laboratory visualization. *Environ. Sci. Technol.*, 36(11):2508–2514, 2002.

[32] M. De Simoni, X. Sanchez-Vila, J. Carrera, and M. W. Saaltink. A mixing ratios-based formulation for multicomponent reactive transport. *Water Resour. Res.*, 43(7):1–10, 2007.

[33] G. Chiogna, O. A. Cirpka, P. Grathwohl, and M. Rolle. Transverse mixing of conservative and reactive tracers in porous media: Quantification through the concepts of flux-related and critical dilution indices. *Water Resour. Res.*, 47(2), 2011.

[34] P. de Anna, T. Le Borgne, M. Dentz, D. Bolster, and P. Davy. Anomalous kinetics in diffusion limited reactions linked to non-Gaussian concentration probability distribution function. *J. Chem. Phys.*, 135:17410, 2011.

[35] P. de Anna. Mixing and reaction in porous media. *PhD thesis - University of Rennes 1*, 2012.

[36] C. J. Werth, O. A. Cirpka, and P. Grathwohl. Enhanced mixing and reaction through flow focusing in heterogeneous porous media. *Water Resour. Res.*, 42(12):1–10, 2006.

[37] P. de Anna, M. Dentz, A.M. Tartakovsky, and T. Le Borgne. The role of filament dynamics in reaction front kinetics. *Geophys. Res. Lett.*, GL060068, 2014.

[38] J. Duplat and E. Villermaux. Mixing by random stirring in confined mixtures. *J. Fluid Mech.*, 617:51–86, 2008.

[39] P. de Anna, J. Jiménez-Martínez, H. Tabuteau, R. Turuban, T. Le Borgne, M. Derrien, and Y. Méheust. Mixing and reaction kinetics in porous media: An experimental pore scale quantification. *Environ. Sci. Technol.*, 48:508–516, 2014.

[40] P. G. de Gennes. Hydrodynamic dispersion in unsaturated porous media. *J. Fluid Mech.*, 136:189–200, 1983.

[41] J. Jiménez-Martínez, P. de de Anna, H. Tabuteau, R. Turuban, T. Le Borgne, and Y. Méheust. Pore-scale mechanisms for the enhancement of mixing in unsaturated porous media and implications for chemical reactions. *Geophys. Res. Lett.*, 42(13):5316–5324, 2015.

[42] G. Nutzmann, S. Maciejewski, and K. Joswig. Estimation of water saturation dependence of dispersion in unsaturated porous media: experiments and modelling analysis. *J. Hydrol.*, 25:565–576, 2002.

[43] K. Hammel and K. Roth. Aproximation of asymptotic dispersivity of conservative solute in unsaturated heterogeneous media with steady state flow. *Water Resour. Res.*, 34(4):709–715, 1998.

[44] H. Fluhler, W. Durner, and M. Flury. Lateral solute mixing processes-A key for understanding field-scale transpor of water and solutes. *Geoderma*, 70:165–183, 1996.

[45] M. Gouet-Kaplan and B. Berkowitz. Measurements of interactions between resident and infiltrating water in a lattice micromodel. *Vadose Zone J.*, 10(2):624–633, 2011.

[46] J. Vanderborght, M. Vanclooster, A. Timmerman, P. Seuntjens, D. Mallants, Kim. D.-J., D. Jacques, L. Hubrechts, C. Gonzalez, J. Feyen, J. Diels, and J. Deckers. Overview of inert tracer experiments in key belgian soil types: Relation between transport and soil morphological an hydraulic properties. *Water Resour. Res.*, 37(12):2837–2888, 2001.

[47] D. Easwaramoorthy, Y.-C. Yu, and H.-J. Huang. Chemiluminescence detection of paracetamol by a luminol-permanganate based reaction. *Anal. Chim. Acta*, 439:95–100, 2001.

[48] Z. Wang, Z. Zhang, and Z. Fu. Sensitive flow-injection chemiluminescence determination of terbutaline sulfate based on enhancement of the luminol-permanganate reaction. *Anal. and Bioanal. Chem.*, 2004.

[49] S. T. Zoumana, S. Xingguang, T. Moussa, and M. M. Anna. Flow-injection chemiluminescence determination of glucose using potassium permanganate-luminol cl system. *International Journal of Life Science Biotechnology and Pharma Research*, 2013.

[50] E. Villermaux and J. Duplat. Coarse-grained scale of turbulent mixtures. *Phys. Rev. Lett.*, 97:144506, 2006.